

MathPhys-Guided Coarse-to-Fine Anomaly Synthesis with SQE-Driven Bi-Level Optimization for Anomaly Detection

Long Qian^{1,2} Bingke Zhu^{1,3} Yingying Chen^{1,3} Ming Tang^{1,2} Jinqiao Wang^{1,2,3}

¹ Foundation Model Research Center, Institute of Automation,
Chinese Academy of Sciences, Beijing, China

² School of Artificial Intelligence, University of Chinese Academy of Sciences, Beijing, China

³ Objecteye Inc., Beijing, China

qianlong2024@ia.ac.cn

{bingke.zhu,yingying.chen,tangm,jqwang}@nlpr.ia.ac.cn

Abstract

Anomaly detection is a crucial task in computer vision, yet collecting real-world defect images is inherently difficult due to the rarity and unpredictability of anomalies. Consequently, researchers have turned to synthetic methods for training data augmentation. However, existing synthetic strategies (e.g., naive cut-and-paste or in-painting) overlook the underlying physical causes of defects, leading to inconsistent, low-fidelity anomalies that hamper model generalization to real-world complexities. In this thesis, we introduced a novel pipeline that generates synthetic anomalies through Math-Physics model guidance, refines them via a Coarse-to-Fine approach and employs a bi-level optimization strategy with a Synthesis Quality Estimator(SQE). By incorporating physical modeling of cracks, corrosion, and deformation, our method produces realistic defect masks, which are subsequently enhanced in two phases. The first stage (npcF) enforces a PDE-based consistency to achieve a globally coherent anomaly structure, while the second stage (npcF++) further improves local fidelity using wavelet transforms and boundary synergy blocks. Additionally, we leverage SQE-driven weighting, ensuring that high-quality synthetic samples receive greater emphasis during training. To validate our approach, we conducted comprehensive experiments on three widely adopted industrial anomaly detection benchmarks: MVTec AD, VisA, and BTAD. Across these datasets, the proposed pipeline achieves state-of-the-art (SOTA) results in both image-AUROC and pixel-AUROC, confirming the effectiveness of our MaPhC2F and BiSQAD.

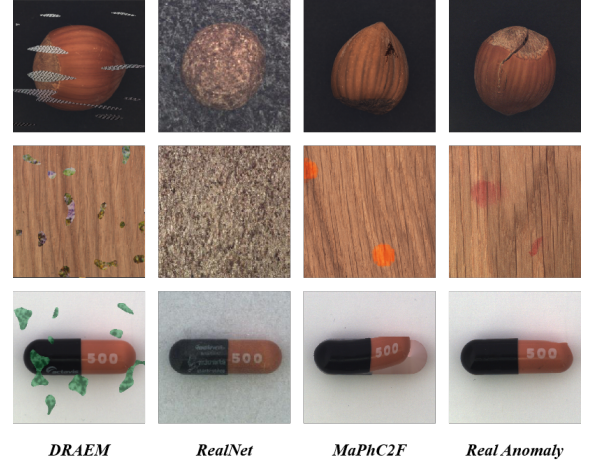


Figure 1. Comparison of different anomaly generation method.

1. Introduction

Recent developments in deep learning have spurred substantial progress in anomaly detection, particularly through techniques that harness synthetic anomalies to compensate for the scarcity and variability of real-world defects. On one hand, self-supervised methods based on simple cut-and-paste perturbations [17] or reverse distillation [5, 9, 26] show that learning “normal” appearance can be highly effective without labeled anomalies. On the other hand, more advanced generation strategies have emerged in the past few years. Diffusion-based approaches [23, 35, 39] and transformer-driven models enable controllable or prompt-guided synthesis of subtle, realistic defects.

Despite the promise of synthetic anomaly data, two critical issues remain unsolved. *First*, conventional synthetic strategies (e.g., simple splicing) often fail to incorporate realistic physical phenomena due to lack of mathematical and

Synthetic Defect Category	Corresponding MVTec AD Anomalies
Cracks	<i>Hazelnut (crack), Leather (cut), Wood (scratch), etc.</i>
Corrosion	<i>Tile (oil), Metal Nut (color), Zipper (rough), etc.</i>
Deformations	<i>Bottle (broken), Capsule (squeeze), Transistor (misplaced), etc.</i>

Table 1. Correspondence between three synthetic anomalies types and real MVTec AD anomalies types

physical model constraints, resulting in anomalies that lack fidelity to genuine defects. *Second*, even if it becomes feasible to generate large volumes of anomalies, the results from previous methods can be of *vastly varying quality*. Some synthesized defects deviate so strongly that they may degrade detection performance when used naively in training. A mechanism to *evaluate* and *selectively emphasize* high-quality synthesized data is thus sorely needed.

To address these challenges, we present a novel framework entitled **MathPhys-Guided Coarse-to-Fine** method and **Bi-Loop SQE-Anomaly Detection**. First, our **MathPhys-Guided Coarse-to-Fine** method, called **MaPhC2F** synthesizes various types of anomalies by leveraging *mathematically inspired models* that follow physical principles. Specifically, we generate defect masks representative of cracks, corrosion, or deformations. These masks are blended into the original image and then refined using a coarse-to-fine pipeline. In the coarse stage, we train an autoencoder-like structure with a mathematical-physics regularization to smooth out inconsistent boundaries. In the fine stage, we adopt wavelet domain operations, synergy blocks at defect boundaries, and advanced feature interplay to produce high-fidelity anomalies. In Fig. 1, we illustrate how existing methods (*DRAEM* [37], *RealNet* [40]) produce anomalies of varying fidelity, while our *MaPhC2F* generates results closer to real anomalies. Tab. 1 lists corresponding anomaly categories from the *MVTec AD* dataset, indicating that these synthetic defect types can effectively represent a broad range of realistic anomalies.

Second, to address the inherently varying fidelity among our coarse-to-fine synthetic anomalies, we introduce a **Bi-Loop SQE-Anomaly Detection** scheme, **BiSQAD**, which unites a *Synthesis Quality Estimator (SQE)* network with a *bi-loop optimization* strategy. Specifically, we freeze a pre-train network to extract global features for each synthetic sample and train only a lightweight final layer in the SQE. During each training epoch, we record the per-sample losses from the main anomaly detection model. These losses, after min-max normalization, serve as pseudo-labels for SQE, indicating the quality of each synthetic example.

In summary, **BiSQAD** follows a meta-learning style bi-loop process. The *inner loop* trains the anomaly detection model on both real and synthetic samples, recording each sample’s loss. Then, in the *outer loop*, the model’s main parameters remain fixed while we update the SQE net-

work (and optionally per-sample weights) based on these recorded losses. Consequently, high-SQE anomalies gain more training influence, while lower-fidelity samples are downweighted, thus guiding the system to focus on the most beneficial synthetic anomalies.

Across three widely recognized industrial benchmarks—*MVTec AD*, *VisA*, and *BTAD*—our framework achieves state-of-the-art performance in both image-level and pixel-level AUROCs, indicating not only strong detection accuracy but also precise defect localization. Additionally, by curating and releasing a large-scale *MaPhC2F Dataset* with 115,987 synthetic images, we further enrich the resources for anomaly detection research.

In essence, these contributions solve two critical problems with existing synthetic anomaly methods: (1) the inability to capture realistic anomalies and (2) the lack of a mechanism to evaluate and selectively focus on higher-quality generated anomalies. Our results demonstrate that integrating physically inspired anomaly masks and adaptive weighting boosts robustness against low-fidelity samples, consequently improving model performance.

We summarize our main contributions as follows:

- We propose a *math-physics guided* approach to anomaly generation (**MaPhC2F**), capturing diverse real-world defects (e.g., cracks, corrosion, deformation) and refining them via a coarse-to-fine process. Furthermore, we provide a **MaPhC2F Dataset** derived from this pipeline.
- We introduce **SQE-driven bi-loop** optimization (**BiSQAD**), which learns to reweight synthetic data based on their fidelity and utility for anomaly detection, dynamically improving consistency to synthetic artifacts.
- Our framework integrates these components into an end-to-end pipeline that scales effectively to industrial-scale datasets. Extensive experiments on multiple benchmarks show **SOTA** performance, demonstrating significant improvements over prior synthetic-based or standard anomaly detection methods.

2. Related Work

Recent years have witnessed a surge of research on synthetic data methods for anomaly detection, drawing upon advances in *generative models*, *self-supervised data augmentation*, and *diffusion-based* approaches.

Self-Supervised Augmentation and Autoencoders. Another line of work employs *autoencoders* and data augmentations to simulate anomalies for self-supervised tasks. *CutPaste* [17] randomly splices image patches onto normal samples to produce pseudo-defects. Follow-up techniques integrate more advanced skills, as in *NSA* [32]. Concurrently, methods like *DRAEM* [37] use an autoencoder combined with a discriminative network, training on images cor-

rupted. Others incorporate knowledge distillation from pre-trained networks [5, 30] to guide reconstruction losses and further refine anomaly detection.

GAN. GAN have traditionally played a key role in synthesizing data for anomaly detection. Early works such as *GANomaly* [1] and *f-AnoGAN* [31] introduced reconstruction-style pipelines, reconstructing normal data and flagging anomalies based on reconstruction discrepancies. Later, *OCGAN* [25] extended these ideas to detection with a latent-space regularization. GAN-based frameworks’ training instability and limited coverage of the anomaly manifold remain open challenges [24].

Diffusion Models. Recently, *diffusion* and *score-based* models have emerged as powerful generators of synthetic anomalies. For example, *AnoDDPM* [35] introduced a denoising diffusion approach to produce subtle artifacts not captured by GANs. Later works leveraged diffusion for both anomaly detection and synthesis, such as *AnomalyDiffusion* [13] and *TransFusion* [8], which jointly learn to generate anomalies and discriminate them from normal data. Additionally, some frameworks use diffusion as a likelihood proxy: if the model requires more steps or a higher denoising cost, the sample may deviate from normality [20, 34].

Out-of-Distribution Detection and Synthetic Outliers. Synthetic data approaches also appear in out-of-distribution (OOD) detection. *Outlier Exposure* [12] first demonstrated that training with artificially introduced outliers improves OOD detection. Subsequently, *VOS* [6] generated virtual outliers in feature space, while *DivOE* [41] extended these ideas to diversify or extrapolate outlier representations. Though these works focus on OOD rather than direct pixel-level anomalies, similar synthetic strategies are used to broaden the training distribution. Meanwhile, large-scale pretraining has facilitated generative architectures for both normal data modeling and anomaly generation [16, 27].

Hybrid Approaches and Advanced Architectures. Beyond pure synthesis or direct detection, new hybrid methods unify generation and anomaly detection. For instance, *RealNet* [40] proposed a feature selection backbone that can incorporate realistic synthetic defects to guide training. *HardSynth* [14], *AnoGen* [10] attempts to generate hard samples that push detectors to improve. Recent augmentation studies, such as *AugmentAD* [18], systematically combine multiple forms of artificial corruption to optimize anomaly detection. Meanwhile, refinement-based approaches (e.g. combining wavelet or PDE constraints [6, 8]) produce higher fidelity anomalies that more closely mimic real anomalies.

In contrast to these prior works, our pipeline leverages a *math-physics* guided approach, focusing on physical processes rather than cut-and-paste. Furthermore, we apply a coarse-to-fine refinement to ensure both globally coherent and locally fine-grained anomalies. Lastly, we introduce a bi-loop optimization technique that reweights synthetic samples based on quality, preventing low-fidelity anomalies from degrading performance. This combination of explicit physical modeling and adaptive weighting distinguishes our method from purely generative or augmentation-based strategies that often lack mechanisms to either model genuine defect or identify inferior synthetic data.

3. Method

3.1. Overview

In Fig. 2, we present a concise overview of our entire framework, highlighting four key components: *BaseModel*, *BiSQAD*, *MaPhC2F*, and the *SynthesisQualityEstimator* (*SQE*). First, *MaPhC2F* produces math-physically informed anomalies via a coarse-to-fine refinement pipeline, which are then fed—together with normal samples—into the *BaseModel* for anomaly detection. Next, *BiSQAD* acts as a bi-loop optimization loop that balances each synthetic sample’s training influence based on the *SQE*’s quality scores. In this way, our approach dynamically emphasizes high-fidelity anomalies and reduces the impact of less beneficial ones, thereby enhancing overall performance.

3.2. MaPhC2F

3.2.1. Math-Physics Guided

In this subsection, we describe how we generate three types of physically inspired anomaly masks—*crack*, *corrosion*, and *deformation*. As a prerequisite, we use an instance segmentation model *SAM* [15] to extract the foreground region corresponding to the relevant item category, ensuring that our subsequent anomaly generation applies only within the object of interest. This way, each physically motivated model operates on a clearly delineated foreground mask, producing realistic anomalies.

Crack Generation We model crack propagation on a 2D plane of size $H \times W$ by iteratively extending “frontiers” in random directions. Let

$$\mathcal{S}(y, x) = \begin{cases} 1, & \text{if pixel } (y, x) \text{ lies on a crack skeleton,} \\ 0, & \text{otherwise.} \end{cases} \quad (1)$$

For each frontier at position (y, x) with movement vector (dy, dx) and remaining steps $M > 0$, we update

$$y_{\text{new}} = y + dy, \quad x_{\text{new}} = x + dx, \quad (2)$$

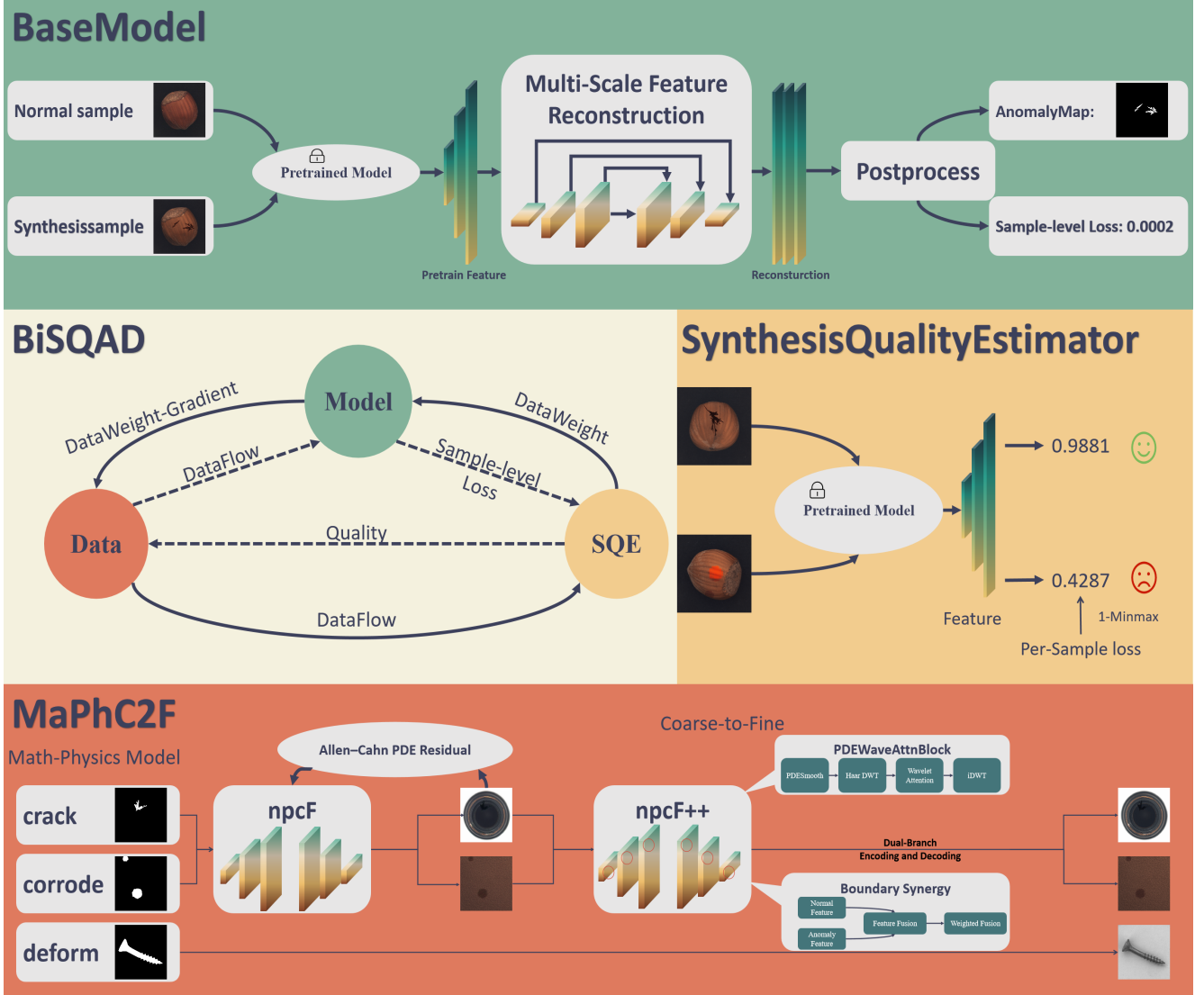


Figure 2. Overall pipeline diagram of our approach. **Top:** The BaseModel combines normal and synthetic samples, yielding anomaly maps and sample-level losses. **Middle:** BiSQAD orchestrates data weight updates and SQE-driven quality assessment, which shows the bi-loop optimization. **Bottom-left:** MaPhC2F refines crack, corrosion, or deformation masks from a math-physics standpoint (npcF → npcF++). **Bottom-right:** The SynthesisQualityEstimator uses a pretrained backbone to compute quality scores from per-sample losses.

then mark $\mathcal{S}(y_{\text{new}}, x_{\text{new}}) = 1$ if it is within the foreground region. With probability p_{branch} , a new branch is spawned by sampling a *branch angle* $\Delta\theta$ in $[-\frac{\pi}{4}, \frac{\pi}{4}]$ and rotating (dy, dx) accordingly. Once a frontier's step count is exhausted or a random stop threshold is met, it terminates. This yields a skeleton that may branch and meander, mimicking real-world crack paths.

Next, to produce a binary crack mask $\mathcal{M}_{\text{crack}}(y, x) \in \{0, 1\}$, we evaluate an exponential threshold around each skeleton pixel based on its distance transform. Let

$$\text{dist}(y, x) = \text{distance_transform}(1 - \mathcal{S}(y, x)), \quad (3)$$

where large $\text{dist}(y, x)$ indicates a point far from the skeleton. We define a local thickness function:

$$w_t(y, x) = w_0 \exp(-\alpha \text{dist}(y, x)) + \varepsilon, \quad (4)$$

where $w_0 > 0$, $\alpha > 0$, and $\varepsilon > 0$ are user-chosen parameters. In parallel, a spatially varying Perlin noise $\nu(y, x)$ is sampled:

$$\nu(y, x) = \text{PN}\left(\frac{y}{H}, \frac{x}{W}\right) \cdot \text{scale}, \quad (5)$$

with PN denoting PerlinNoise(\cdot) and $\text{scale} > 0$. If

$$\text{dist}(y, x) + \nu(y, x) < w_t(y, x), \quad (6)$$

then $\mathcal{M}_{\text{crack}}(y, x) = 1$; otherwise 0. Finally, morphological smoothing (e.g. closing+opening) is applied. This procedure ensures that regions near the skeleton remain inside the crack, whereas distant or noisy regions are excluded.

Corrosion Generation We simulate blocky or aggregated corrosion patterns by randomly placing polygons within the foreground mask and then growing them via boundary expansions. Let $\mathcal{M}_{\text{corrode}}(y, x)$ be the corrosion mask. We begin by sampling k random polygons, each clipped to the foreground. These polygons may overlap (with probability p_{overlap}) or be unioned otherwise. In each polygon, we fill internal pixels to 1. We then perform a local BFS-like boundary growth for N_{growth} iterations, turning boundary pixels into mask pixels with probability p_{grow} . After morphological closing, an optional Perlin noise step randomly erodes boundary pixels:

$$\mathcal{M}_{\text{corrode}}(y, x) = \begin{cases} 0, & \text{if } \nu\left(\frac{y}{H}, \frac{x}{W}\right) > \rho, \\ \mathcal{M}_{\text{corrode}}(y, x), & \text{otherwise,} \end{cases} \quad (7)$$

where ρ is a threshold controlling edge breakage. The result is a connected mask that resembles corrosive patches.

Deformation Generation via Thin-Plate Spline To simulate local warping or bending, we adopt a thin-plate spline (TPS) approach. Let $\mathcal{M}_{\text{deform}}(y, x)$ represent the region to be deformed. After extracting a bounding box on the foreground, we sample *control points* $\{(r_i, c_i)\}_{i=1}^m$ along $\mathcal{M}_{\text{deform}}$ and displace them by random offsets. An RBF-based TPS function [11] is then computed to map each pixel (y, x) to a new location (y', x') . Formally,

$$(x', y') = (x, y) - [\text{Rbf}_x(x, y), \text{Rbf}_y(x, y)], \quad (8)$$

where Rbf_x and Rbf_y are trained via radial basis functions to interpolate the control points. We apply this mapping to both the image and the mask, optionally inpainting the removed object area before overlay. This yields realistic local distortions akin to dents or folds.

Overall, these three math-physics guided processes—crack, corrosion, and deformation—produce diverse and physically plausible anomaly masks. In the following subsections, these masks serve as inputs to our coarse-to-fine refinement pipeline, ultimately generating high-fidelity anomalies for subsequent model training.

3.2.2. npcF (Coarse Refinement)

The first stage of our coarse-to-fine synthesis, **npcF**, applies a wide-resnet-based autoencoder together with *Allen–Cahn PDE* constraints [2, 36], and other auxiliary terms to refine the raw anomaly masks into a more coherent form. In essence, we aim to smooth out unnatural boundaries, avoid extreme color artifacts, and preserve contextual cues before proceeding to the fine-grained stage.

Allen–Cahn PDE Residual. Let $\mathbf{u} \in \mathbb{R}^{B \times 3 \times H \times W}$ represent a batch of reconstructed images output by the autoencoder. We adopt a pixel-domain Allen–Cahn PDE term to enforce local consistency in the *anomaly* regions:

$$\text{Res}_{\text{AC}}(\mathbf{u}) = \varepsilon^2 \nabla^2 \mathbf{u} - (\mathbf{u}^3 - \mathbf{u}), \quad (9)$$

where ∇^2 denotes the discrete 2D Laplacian operator, and $\varepsilon > 0$ is a parameter that controls the diffusion strength. Concretely, if \mathbf{M}_{anom} is a binary anomaly mask (1 in defect pixels, 0 otherwise), then we apply the following Allen–Cahn loss restricted to anomaly regions:

$$\ell_{\text{pde}} = \|\text{Res}_{\text{AC}}(\mathbf{u}) \odot \mathbf{M}_{\text{anom}}\|^2, \quad (10)$$

where \odot denotes elementwise multiplication.

Reconstruction & Regularization In *npcf*, we use two distinct reconstruction terms—one targeting pixels outside the anomaly mask and one for anomalous regions—along with several auxiliary regularizers (e.g., TV, color prior, perceptual loss). These ensure that reconstructed anomalies remain visually consistent. *For the precise definitions, please see the supplementary material.*

3.2.3. npcF++ (Fine-Grained Refinement)

After obtaining a coarse anomaly approximation via *npcf*, we further refine local details, boundary transitions, and high-frequency texture in a process we call **npcF++**. This stage integrates *wavelet-domain attention*, *PDE-based enhancement*, and a *boundary synergy* mechanism.

Wavelet-PDE Attentive Blocks, Boundary Synergy, and Dual-Branch Design We refine feature maps via a combination of *PDEWaveAttnBlock* (which fuses *PDE smoothing* and wavelet-based subband transformations) and a *RegionSynergyBlock* that aligns normal/anomaly features around boundary regions. These modules are organized in dual-branch encoders for normal and anomaly inputs, followed by a shared bottleneck and decoding path. The final output is a 3×3 convolution plus sigmoid. *For complete equations, including how wavelet decomposition (DWT/iDWT) and boundary cross-attention are integrated across multiple scales, see the supplementary material.*

Loss Functions. Let $\mathbf{u} \in \mathbb{R}^{B \times 3 \times H \times W}$ represent a batch of reconstructed images output by the autoencoder. We rely on a *region loss* and a *wavelet high-frequency penalty*:

$$\begin{aligned} \ell_{\text{region}} = & \|\mathbf{u} \odot \mathbf{M}_{\text{norm}} - (\mathbf{x}_{\text{orig}} \odot \mathbf{M}_{\text{norm}})\|_1 \\ & + \beta \left(\|\mathbf{u} \odot \mathbf{M}_{\text{anom}} - (\mathbf{x}_{\text{b1}} \odot \mathbf{M}_{\text{anom}})\|_1 \right. \\ & \left. + \delta \|\mathbf{u} - \mathbf{x}_{\text{orig}}\|_2^2 \right) \end{aligned} \quad (11)$$

Category		DSR [38]	CutPaste [17]	DRAEM [37]	AnomalyDiffusion [13]	RD++ [33]	RealNet [40]	BiSQAD
Object	Bottle	99.6/98.8	100 /99.1	99.2/97.8	99.8/99.4	100 /98.8	100 /99.3	100/99.6
	Cable	95.3/97.7	96.4/96.2	91.8/94.7	100 /99.2	99.3/98.4	99.2/98.1	99.6/ 99.6
	Capsule	98.3/91.0	98.5/99.1	98.5/94.3	99.7 /98.8	99.0/98.8	99.6/99.3	99.4/ 99.6
	Hazelnut	97.7/99.1	100 /99.0	100 /99.7	99.8/99.8	100 /99.2	100 /99.8	100/99.9
	Metal Nut	99.1/94.1	99.9/98.0	98.7/99.5	100 /99.8	100 /98.1	99.7/98.6	99.7/99.4
	Pill	98.9/94.2	97.2/99.0	98.9/97.6	98.0/ 99.8	98.4/98.3	99.1 /99.0	98.2/ 99.8
	Screw	95.9/98.1	92.7/98.5	93.9/97.6	96.8/97.0	98.9 /99.7	98.8/99.5	98.1/ 99.8
	Toothbrush	100/99.5	99.2/98.9	100 /98.1	100 /99.2	100 /99.1	99.4/98.7	99.4/98.7
	Transistor	96.3/80.3	99.4/96.3	93.1/90.9	100/99.3	98.5/94.3	100 /98.0	99.4/98.1
	Zipper	98.5/98.4	99.6/98.0	100 /98.8	99.9/99.4	98.6/98.8	99.8/99.2	100/99.7
Texture	Carpet	99.6/96.0	99.2/98.4	97.0/95.5	96.7/98.6	100 /99.2	99.8/99.2	99.7/ 99.9
	Grid	100 /99.6	100 /99.2	99.9/99.7	98.4/98.3	100 /99.3	100 /99.5	100/99.8
	Leather	99.3/99.5	100 /99.4	100 /98.6	100/99.8	100 /99.5	100/99.8	100/99.8
	Tile	100 /98.6	99.9/97.6	99.6/99.2	100 /99.2	99.7/96.6	99.9/99.4	99.9/ 99.7
	Wood	94.7/91.5	99.0/95.0	99.1/96.4	98.4/ 98.9	99.3 /95.8	99.2/98.2	98.3/98.8
Avg.		98.2/95.8	98.7/98.1	99.2/99.1	98.5/97.7	99.4/98.3	99.6 /99.0	99.5/ 99.5

Table 2. Performance comparison across different SOTA methods on *MVTec AD* dataset. **Bold text** indicates the best performance among all method. The values in the form of xx/xx represent *image-level AUROC* / *pixel-level AUROC*.

where $\mathbf{M}_{\text{norm}} = 1 - \mathbf{M}_{\text{anom}}$, \mathbf{x}_{b1} is the coarse anomaly image, and β, δ are weighting factors. Additionally, we penalize high-frequency edges in anomaly regions via:

$$\ell_{\text{waveHF}} = \|\text{convHF}(\mathbf{u}) \odot \mathbf{M}_{\text{anom}}\|_1, \quad (12)$$

where $\text{convHF}(\cdot)$ is a 3×3 Laplacian kernel [21]. The total loss is then $\ell_{\text{region}} + \ell_{\text{waveHF}}$.

3.3. BiSQAD

With our refined anomalies in place, we now address the problem of *uneven anomaly quality*. Some synthetic samples closely match real defects, whereas others may hinder detection if used indiscriminately. We thus propose a bi-loop optimization strategy, **BiSQAD**, that leverages a *Synthesis Quality Estimator (SQE)* to dynamically weight each sample’s contribution, combined with a optional *strict second-order* meta-learning update for data weights.

3.3.1. SQE

We define a scoring function $q_i \in [0, 1]$ for each synthetic sample i . Let \mathbf{x}_{sqe} be the normalized image patch fed to a frozen backbone WideResNet-50 followed by a learnable final layer:

$$q_i = \sigma\left(\text{fc}\left(\text{FeatExtract}(\mathbf{x}_{\text{sqe}})\right)\right), \quad (13)$$

where $\sigma(\cdot)$ is a sigmoid function. To train SQE *without* manual labels, we observe basemodel’s per-sample losses ℓ_i during training. The target quality for sample i is

$$y_i = 1.0 - \frac{\ell_i - \min(\ell)}{\max(\ell) - \min(\ell) + \varepsilon}, \quad (14)$$

where ε is a small constant preventing division by zero. We then regress q_i toward y_i using an ℓ_2 loss. As a result, synthetic anomalies that produce higher loss (worse detection performance) are assigned lower quality q_i , and vice versa.

3.3.2. Bi-Loop Optimization

Inner Loop: Weighted Training. During normal training on a batch, each sample i is assigned a dynamic weight

$$w_i = \lambda_{\text{sqe}} q_i + \lambda_{\text{bi}} d_i, \quad (15)$$

where d_i is an optional learnable data weight and $\lambda_{\text{sqe}}, \lambda_{\text{bi}}$ are hyperparameters. If $\lambda_{\text{bi}} = 0$, only SQE-based weighting remains. We scale the main detection loss by w_i , generating an updated model parameter set θ' .

Outer Loop: Weights’ Learning. At the end of each epoch, we refine a final SQE layer as shown in Sec. 3.3.1 and the sample-level data weights (d_i) using a validation-based objective (e.g. AUC loss). This optional, strictly second-order MAML step temporarily freezes the main model θ' and backpropagates through the inner-loop graph to adjust $\{d_i\}$. *Further implementation details and full equations appear in the supplementary material.*

In summary, *BiSQAD* ties together an online SQE with a second-order meta-learning loop. This synergy ensures that training continuously promotes anomalies beneficial to the detector and curbs those that risk hurting final performance.

Category	<i>DSR</i> [4]	<i>SimpleNet</i> [19]	<i>DRAEM</i> [37]	<i>PatchCore</i> [29]	<i>RD++</i> [33]	<i>RealNet</i> [40]	<i>BiSQAD</i>
<i>Candle</i>	86.4/79.7	92.3/97.7	91.8/96.6	98.6 /99.5	96.4/98.6	96.1/99.1	96.5/ 99.8
<i>Capsules</i>	93.4/74.5	76.2/94.6	74.7/98.5	81.6/ 99.5	92.1/99.4	93.2/98.7	95.4 /98.6
<i>Cashew</i>	85.2/61.5	94.1/99.4	95.1/83.5	97.3/98.9	97.8 /95.8	97.8 /98.3	97.1/ 99.9
<i>Chewinggum</i>	97.2/58.2	97.1/97.0	94.8/96.8	99.1/99.1	96.4/99.0	99.9 / 99.8	99.5/99.7
<i>Fryum</i>	93.0/65.5	88.0/93.5	97.4 /87.2	96.2/93.8	95.8/94.3	97.1/ 96.2	96.2/95.0
<i>Macaroni1</i>	91.7/57.7	84.7/95.4	97.2/ 99.9	97.5/99.8	94.0/99.7	99.8 / 99.9	96.5/ 99.9
<i>Macaroni2</i>	79.0/52.2	75.0/83.8	85.0/99.2	78.1/99.1	88.0/87.7	95.2/ 99.6	96.6 /98.4
<i>PCB1</i>	89.1/61.3	93.4/99.1	47.6/88.7	98.5 / 99.9	97.0/75.0	98.5 /99.7	98.1/ 99.9
<i>PCB2</i>	96.4/84.9	90.0/94.8	89.8/91.3	97.3/99.0	97.2/64.8	97.6 /98.0	96.5/ 99.7
<i>PCB3</i>	97.0/79.5	91.3/98.2	92.0/98.0	97.9/99.2	96.8/95.5	99.1 /98.8	98.8/ 99.9
<i>PCB4</i>	98.5/62.1	99.1/94.5	98.6/96.8	99.6/98.6	99.8 /92.8	99.7/98.6	99.6/ 99.8
<i>Pipe fryum</i>	94.3/80.5	89.0/95.3	100.0 /85.8	99.8/99.1	99.6/92.0	99.9/99.2	98.3/ 99.8
Avg.	91.8/68.1	89.2/95.3	88.7/93.5	95.1/98.8	95.9/90.1	97.8 /98.8	97.4/ 99.2

Table 3. Performance comparison across different SOTA methods on *VisA* dataset. **Bold text** indicates the best performance among all method. The values in the form of *xx/xx* represent *image-level AUROC* / *pixel-level AUROC*.

Category	<i>SimpleNet</i> [19]	<i>SPADE</i> [4]	<i>RD</i> [5]	<i>RD++</i> [33]	<i>RealNet</i> [40]	<i>BiSQAD</i>
<i>01</i>	96.4/90.3	91.4/97.3	97.9/99.3	96.8/96.2	100 / 98.2	99.8/98.0
<i>02</i>	75.2/48.9	71.4/94.4	86.0/97.7	90.1 /96.4	88.6/96.3	89.1/ 96.6
<i>03</i>	99.3/97.2	99.9/99.1	99.7/94.2	100 / 99.7	99.6/99.4	99.8/99.6
Avg.	90.3/78.8	87.6/96.9	94.5/97.1	95.6/97.4	96.1/97.9	96.3 / 98.1

Table 4. Performance comparison across different SOTA methods on *BTAD* dataset. **Bold text** indicates the best performance among all method. The values in the form of *xx/xx* represent *image-level AUROC* / *pixel-level AUROC*.

4. Experiment

4.1. Experiment Setup

Datasets. In this work, we evaluate our approach on three popular anomaly detection datasets: *MVTec AD* [3], *VisA* [42] and *BTAD* [22]. *MVTec AD* contains 5,354 images across 15 categories, *VisA* comprises 10,821 images spanning 12 categories and *BTAD* contains 2540 images of 3 industrial products.

Implementation details. For most stages of our pipeline, we set the batch size to 32 and train for about 200 epochs on the coarse refinement(*npcF*) and 50 epochs on the fine refinement(*npcF++*). During training, images are resized to 512×512 resolution.

Regarding the math-physics anomaly generation, parameters such as crack thickness, corrosion polygon size, and TPS offset ranges are randomly sampled to ensure a diverse set of anomalies. In *npcF++*, the default window size is 16, used by the wavelet-based synergy blocks.

Finally, during the bi-level SQE training, the SQE network leverages a frozen *WideResNet50-v2* backbone. We

only train its final linear layer using *AdamW* at a learning rate of 10^{-4} for $2 \sim 10$ epochs per outer loop iteration. For data weighting, we either rely on the SQE score alone or optionally combine it with a separate learnable data weight.

We quantify anomaly detection performance using the standard metrics of image-level and pixel-level AUROC.

4.2. MaPhC2F Dataset

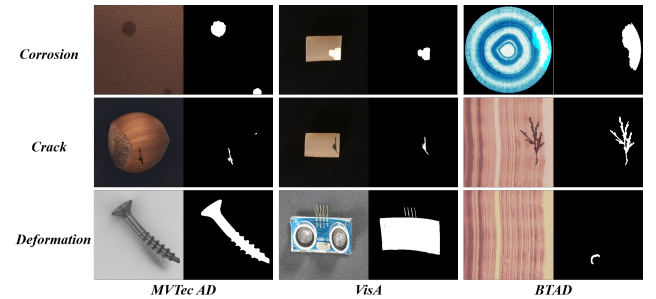


Figure 3. Visualization of three math-physics anomaly types in our **MaPhC2F Dataset**: (Up) *Corrosion-based*, (Center) *Crack-based*, and (Down) *TPS-based* defects.

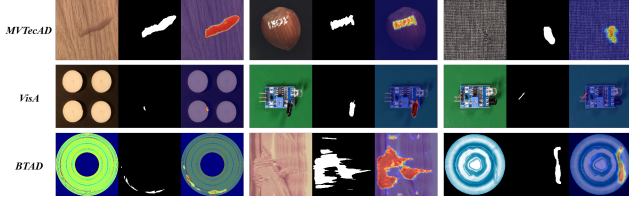


Figure 4. Visualization examples of anomaly detection results on (Up) *MVTec AD*, (Center) *VisA*, and (Down) *BTAD*.

We introduce the ***MaPhC2F Dataset***, a large-scale synthetic anomaly collection generated via our math-physics guided pipeline. It spans 115,987 images across 30 object categories, each refined through the coarse-to-fine approach described in Sec. 3.2.2–Sec. 3.2.3. As depicted in Fig. 3, the dataset includes three representative anomaly types—*corrosion*, *cracks*, and *TPS (thin-plate spline) deformations*—covering diverse shapes, boundary transitions, and intensities. This extensive coverage ensures that the *MaPhC2F Dataset* can benefit a wide range of anomaly detection scenarios. We provide additional visual examples, along with detailed statistics of the dataset, in the supplementary material.

4.3. Comparison with SOTAs

We benchmark our method on three prominent industrial anomaly detection datasets: *MVTec AD*, *VisA*, and *BTAD*. As shown in Tab. 2, *BiSQAD* achieves an overall 99.5%/99.5% (image-/pixel-level AUROC) on *MVTec AD*, outperforming or matching other leading approaches in both *object* and *texture* categories. In Tab. 3, our method obtains an average 97.4%/99.2% on *VisA*, underscoring robust detection accuracy and boundary localization across diverse items. Tab. 4 reports results on *BTAD*, where *BiSQAD* again surpasses recent baselines, achieving 96.3%/98.1%.

Crucially, our *pixel-level AUROC* attains a notable uplift over prior methods, indicating refined localization of defects and sharper boundary consistency. In some cases, pixel-level performance improves by +1.5–2% compared to competing systems. Overall, *BiSQAD* consistently outperforms existing state-of-the-art methods on both image- and pixel-level metrics. On *MVTec AD* (Tab. 2), it exceeds *RealNet* and *RD++* in nearly all categories, while on *VisA* (Tab. 3) it demonstrates strong adaptability in challenging scenarios, surpassing *DRAEM* and *RealNet*. Meanwhile, *BTAD* results (Tab. 4) reaffirm the method’s robustness, securing top-tier AUROCs across multiple defect types. This consistent performance highlights the versatility and effectiveness of our approach for industrial anomaly detection.

Visualization examples of anomaly detection on *MVTec AD*, *VisA*, and *BTAD* are presented in Fig. 4. These results highlight the method’s fine-grained localization capabilities, consistently identifying subtle boundary details

and diverse defect patterns. Additional examples in the supplementary materials further confirm the robustness and SOTA-level performance of our approach across various anomaly types.

4.4. Ablation Study

Method Variant	Image-AUROC	Pixel-AUROC	Comments
(1) <i>npcF</i> only	94.9	95.4	-
(2) +PDEWave	97.3(+2.4)	97.2(+1.8)	partial fine stage
(3) Full <i>npcF++</i>	99.5(+2.2)	99.5(+2.3)	PDEwave + synergy

Table 5. Ablation results for *npcF++* in *MaPhC2F* on *MVTec AD* dataset.

<i>SQE</i> Variant	Image-AUROC	Pixel-AUROC	Comments
No <i>SQE</i>	95.6	96.4	Default Weight
+ <i>SQE</i>	99.5(+3.9)	99.5(+3.1)	Score Weight

Table 6. Ablation results for *SQE* in *BiSQAD* on *MVTec AD* dataset.

We conduct ablation experiments on two core elements of our pipeline: *npcF++* (within *MaPhC2F*) and the *SQE*-driven reweighting in *BiSQAD*. Tab. 5 illustrates the benefit of refining our coarse stage (*npcF*) with PDEWave-based operations and synergy blocks. Transitioning from *npcF* alone (row 1) to a partial refinement (+PDEWave, row 2) yields +2.4% in image-level AUROC and +1.8% in pixel-level AUROC. By enabling the complete *npcF++* pipeline (row 3), we observe an additional +2.2% and +2.3% gain, respectively, indicating that synergy blocks deliver fine-grained improvements in anomaly realism.

Next, Table 6 examines how our Synthesis Quality Estimator (*SQE*) influences performance within *BiSQAD*. Disabling *SQE* (row 1) reduces overall accuracy, whereas applying *SQE*-based score weighting (row 2) improves image-level AUROC by +3.9% and pixel-level AUROC by +3.1%. This confirms that emphasizing high-quality synthetic anomalies significantly boosts detection metrics.

Altogether, these results confirm that *npcF++* notably elevates the realism of generated anomalies by capturing subtle textures and boundary details, while the *SQE*-driven weighting mechanism effectively mitigates the impact of low-fidelity synthetic samples. Consequently, the overall detection pipeline is rendered more robust and better aligned with real-world defect scenarios.

5. Conclusion

In this paper, we have presented a comprehensive pipeline for anomaly detection that combines physically grounded anomaly generation (*MaPhC2F*) with adaptive reweighting via a second-order optimization scheme (*BiSQAD*). By

synthesizing diverse defects (cracks, corrosion, deformation) and refining them through a two-stage (coarse-to-fine) process, **MaPhC2F** yields high-fidelity anomalies and also contributes a large-scale *MaPhC2F Dataset* of 115,987 synthetic images spanning 30 object categories. Moreover, our **SQE-driven bi-loop** framework dynamically assesses the fidelity of these generated anomalies, assigning higher importance to high-quality samples. Extensive experiments on multiple benchmark datasets, including MVTec AD, VisA, and BTAD, demonstrate that our method achieves state-of-the-art performance in both image- and pixel-level AUROCs, significantly outperforming previous synthetic-based or conventional anomaly detection approaches.

References

- [1] Samet Akcay, Amir Atapour-Abarghouei, and Toby P. Breckon. GANomaly: Semi-supervised anomaly detection via adversarial training. In *Proc. of ACCV Workshops*, 2018. 3
- [2] Samuel M Allen and John W Cahn. A microscopic theory for antiphase boundary motion and its application to antiphase domain coarsening. *Acta metallurgica*, 27(6):1085–1095, 1979. 5
- [3] Paul Bergmann, Michael Fauser, David Sattlegger, and Carsten Steger. Mvtec ad—a comprehensive real-world dataset for unsupervised anomaly detection. In *Proceedings of the IEEE/CVF conference on computer vision and pattern recognition*, pages 9592–9600, 2019. 7
- [4] Niv Cohen and Yedid Hoshen. Sub-image anomaly detection with deep pyramid correspondences. *arXiv preprint arXiv:2005.02357*, 2020. 7
- [5] Hanqiu Deng and Xingyu Li. Anomaly detection via reverse distillation from one-class embedding. In *Proc. of CVPR*, pages 9737–9746, 2022. 1, 3, 7
- [6] Xuefeng Du, Zhaoning Wang, Mu Cai, and Yixuan Li. VOS: Learning what you don’t know by virtual outlier synthesis. In *Proc. of ICLR*, 2022. 3
- [7] Chelsea Finn, Pieter Abbeel, and Sergey Levine. Model-agnostic meta-learning for fast adaptation of deep networks. *CoRR*, abs/1703.03400, 2017. 2
- [8] Matic Fučka, Vitjan Zavrtanik, and Danijel Skočaj. Transfusion – a transparency-based diffusion model for anomaly detection. In *Proc. of ECCV (35)*, pages 91–108, 2024. 3
- [9] Zhihao Gu, Jiangning Zhang, Liang Liu, Xu Chen, Jinlong Peng, Zhenye Gan, Guannan Jiang, Annan Shu, Yabiao Wang, and Lizhuang Ma. Rethinking reverse distillation for multi-modal anomaly detection. In *Proceedings of the AAAI Conference on Artificial Intelligence*, pages 8445–8453, 2024. 1
- [10] Guan Gui, Bin-Bin Gao, Jun Liu, Chengjie Wang, and Yunsheng Wu. Few-shot anomaly-driven generation for anomaly classification and segmentation. In *Proc. of ECCV 2024*, 2024. 3
- [11] Rolland L. Hardy. Multiquadric equations of topography and other irregular surfaces. *Journal of Geophysical Research (1896-1977)*, 76(8):1905–1915, 1971. 5
- [12] Dan Hendrycks, Mantas Mazeika, and Thomas Dietterich. Deep anomaly detection with outlier exposure. In *Proc. of ICLR*, 2019. 3
- [13] Teng Hu, Jiangning Zhang, Ran Yi, Yuzhen Du, Xu Chen, Liang Liu, Yabiao Wang, and Chengjie Wang. Anomalydiffusion: Few-shot anomaly image generation with diffusion model. In *Proc. of AAAI*, pages 8526–8534, 2024. 3, 6
- [14] Hyuntae Kim and Changhee Lee. Enhancing anomaly detection via generating diversified and hard-to-distinguish synthetic anomalies. In *Proc. of ACM CIKM*, pages 2542–2551, 2024. 3
- [15] Alexander Kirillov, Eric Mintun, Nikhila Ravi, Hanzi Mao, Chloe Rolland, Laura Gustafson, Tete Xiao, Spencer Whitehead, Alexander C. Berg, Wan-Yen Lo, Piotr Dollár, and Ross Girshick. Segment anything. *arXiv:2304.02643*, 2023. 3
- [16] Mingyu Lee and Jongwon Choi. Text-guided variational image generation for industrial anomaly detection and segmentation. In *Proc. of CVPR*, 2024. 3
- [17] Chun-Liang Li, Kihyuk Sohn, Jinsung Yoon, and Tomas Pfister. Cutpaste: Self-supervised learning for anomaly detection and localization. In *Proceedings of the IEEE/CVF conference on computer vision and pattern recognition*, pages 9664–9674, 2021. 1, 2, 6
- [18] Jiang Lin and Yaping Yan. A comprehensive augmentation framework for anomaly detection. In *Proc. of AAAI*, pages 8743–8750, 2024. 3
- [19] Zhikang Liu, Yiming Zhou, Yuansheng Xu, and Zilei Wang. Simplenet: A simple network for image anomaly detection and localization, 2023. 7
- [20] Victor Liversnoche, Vineet Jain, Yashar Hezaveh, and Siamak Ravanbakhsh. On diffusion modeling for anomaly detection. In *Proc. of ICLR*, 2024. 3
- [21] David Marr and Ellen Hildreth. Theory of edge detection. *Proceedings of the Royal Society of London. Series B. Biological Sciences*, 207(1167):187–217, 1980. 6
- [22] Pankaj Mishra, Riccardo Verk, Daniele Fornasier, Claudio Piciarelli, and Gian Luca Foresti. Vt-adl: A vision transformer network for image anomaly detection and localization. In *2021 IEEE 30th International Symposium on Industrial Electronics (ISIE)*, pages 01–06, 2021. 7
- [23] Arian Mousakhan, Thomas Brox, and Jawad Tayyub. Anomaly detection with conditioned denoising diffusion models. *arXiv preprint arXiv:2305.15956*, 2023. 1
- [24] Guansong Pang, Chunhua Shen, Longbing Cao, and Anton van den Hengel. Deep learning for anomaly detection: A review. *ACM Computing Surveys*, 54(2):1–38, 2021. 3
- [25] Pramuditha Perera, Rajvindra Nath, Hemanth Venkateswara, Sethuraman Panchanathan, and Vishal M. Patel. OCGAN: One-class novelty detection using gans with constrained latent representations. In *Proc. of CVPR*, pages 2898–2906, 2019. 3
- [26] Long Qian, Bingke Zhu, Yingying Chen, Ming Tang, and Jinqiao Wang. Friend or foe? harnessing controllable overfitting for anomaly detection. *arXiv preprint arXiv:2412.00560*, 2024. 1

- [27] Hezhe Qiao, Qingsong Wen, Xiaoli Li, Ee-Peng Lim, and Guansong Pang. Generative semi-supervised graph anomaly detection. In *Advances in Neural Information Processing Systems (NeurIPS)* 37, 2024. 3
- [28] Aravind Rajeswaran, Chelsea Finn, Sham M. Kakade, and Sergey Levine. Meta-learning with implicit gradients. *CoRR*, abs/1909.04630, 2019. 2
- [29] Karsten Roth, Latha Pemula, Joaquin Zepeda, Bernhard Schölkopf, Thomas Brox, and Peter Gehler. Towards total recall in industrial anomaly detection: Feature memory readers. In *Proc. of CVPR*, pages 14318–14328, 2022. 7
- [30] Mahdi Salehi, Yun Fu, Octavia Camps, and Mario Sznaiier. Multiresolution knowledge distillation for anomaly detection. In *Proc. of CVPR*, pages 14902–14912, 2021. 3
- [31] Thomas Schlegl, Philipp Seebock, Sebastian M. Waldstein, Georg Langs, and Ursula Schmidt-Erfurth. f-AnoGAN: Fast unsupervised anomaly detection with generative adversarial networks. *Medical Image Analysis*, 54:30–44, 2019. 3
- [32] Hannah M. Schlüter, Jeremy Tan, Benjamin Hou, and Bernhard Kainz. Natural synthetic anomalies for self-supervised anomaly detection and localization. In *Proc. of ECCV*, pages 474–489, 2022. 2
- [33] Tran Dinh Tien, Anh Tuan Nguyen, Nguyen Hoang Tran, Ta Duc Huy, Soan T.M. Duong, Chanh D. Tr. Nguyen, and Steven Q. H. Truong. Revisiting reverse distillation for anomaly detection. In *Proceedings of the IEEE/CVF Conference on Computer Vision and Pattern Recognition (CVPR)*, pages 24511–24520, 2023. 6, 7
- [34] Julia Wolleb, Florentin Bieder, Robin Sandkühler, and Philippe C. Cattin. Diffusion models for medical anomaly detection. In *Proc. of MICCAI*, pages 35–46, 2022. 3
- [35] Julian Wyatt, Adam D. Leach, Sebastian M. Schmon, and Chris G. Willcocks. AnoDDPM: Anomaly detection with denoising diffusion probabilistic models using simplex noise. In *Proc. of CVPR Workshops*, pages 650–656, 2022. 1, 3
- [36] Zixue Xiang, Wei Peng, Xu Liu, and Wen Yao. Self-adaptive loss balanced physics-informed neural networks. *Neurocomputing*, 496:11–34, 2022. 5
- [37] Vitjan Zavrtanik, Matej Kristan, and Danijel Skočaj. DRÆM: A discriminatively trained reconstruction embedding for surface anomaly detection. In *Proc. of ICCV*, pages 8330–8339, 2021. 2, 6, 7
- [38] Vitjan Zavrtanik, Matej Kristan, and Danijel Skočaj. Dsr – a dual subspace re-projection network for surface anomaly detection. In *Computer Vision – ECCV 2022*, pages 539–554, Cham, 2022. Springer Nature Switzerland. 6
- [39] Xinyi Zhang, Naiqi Li, Jiawei Li, Tao Dai, Yong Jiang, and Shu-Tao Xia. Unsupervised surface anomaly detection with diffusion probabilistic model. In *Proceedings of the IEEE/CVF International Conference on Computer Vision (ICCV)*, pages 6782–6791, 2023. 1
- [40] Ximiao Zhang, Min Xu, and Xiuzhuang Zhou. Realnet: A feature selection network with realistic synthetic anomaly for anomaly detection. In *Proceedings of the IEEE/CVF Conference on Computer Vision and Pattern Recognition (CVPR)*, 2024. 2, 3, 6, 7
- [41] Jianing Zhu, Yu Geng, Jiangchao Yao, Tongliang Liu, Gang Niu, Masashi Sugiyama, and Bo Han. Diversified outlier exposure for out-of-distribution detection via informative extrapolation. In *Advances in Neural Information Processing Systems (NeurIPS)* 36, 2023. 3
- [42] Yang Zou, Jongheon Jeong, Latha Pemula, Dongqing Zhang, and Onkar Dabeer. Spot-the-difference self-supervised pre-training for anomaly detection and segmentation. In *European Conference on Computer Vision*, pages 392–408. Springer, 2022. 7

Appendix

6. Additional Theoretical and Implementation Details

6.1. npcF Reconstruction & Regularization Details

Let $\mathbf{u} \in \mathbb{R}^{B \times 3 \times H \times W}$ represent a batch of reconstructed images output by the autoencoder.

Reconstruction Objectives. Since *npcF* performs a coarse refinement via an autoencoder, we divide the reconstruction loss into two subsets:

1. **Normal region reconstruction:** For pixels outside the anomaly mask, we make \mathbf{u} match \mathbf{x} :

$$\ell_{\text{rec}}^{\text{normal}} = \|(\mathbf{u} - \mathbf{x}) \odot (1 - \mathbf{M}_{\text{anom}})\|_2^2. \quad (16)$$

2. **Anomaly region reconstruction:** For pixels within the anomaly mask, we do a similar reconstruction penalty:

$$\ell_{\text{rec}}^{\text{anom}} = \|(\mathbf{u} - \mathbf{x}) \odot \mathbf{M}_{\text{anom}}\|_2^2. \quad (17)$$

This separation ensures that normal pixels are trained to preserve the input, while anomalous pixels can deviate in a controlled manner.

Additional Regularization. To further guide the reconstruction:

- **Total Variation (TV)** reduces high-frequency noise:

$$\ell_{\text{tv}} = \sum_{c=1}^3 \|\nabla_h(\mathbf{u}_c)\|_1 + \|\nabla_w(\mathbf{u}_c)\|_1, \quad (18)$$

with ∇_h, ∇_w denoting finite differences along spatial axes.

- **Color Prior:** For anomaly pixels, we encourage \mathbf{u} to stay close to a math-physics guided color reference \mathbf{z} :

$$\ell_{\text{color}} = \|\mathbf{u} \odot \mathbf{M}_{\text{anom}} - \mathbf{z}\|_2^2. \quad (19)$$

- **Perceptual Loss:** If a pretrained *VGG* feature extractor ψ is available, we match the feature maps of \mathbf{u} and \mathbf{x} , focusing on anomaly pixels only:

$$\ell_{\text{perc}} = \|\psi(\mathbf{u} \odot \mathbf{M}_{\text{anom}}) - \psi(\mathbf{x} \odot \mathbf{M}_{\text{anom}})\|_2^2. \quad (20)$$

Overall Training Objective. We sum up the above terms with corresponding coefficients λ . to form the total *npcF* loss:

$$\mathcal{L}_{\text{npcF}} = \ell_{\text{rec}}^{\text{normal}} + \lambda_{\text{anom}} \ell_{\text{rec}}^{\text{anom}} + \lambda_{\text{pde}} \ell_{\text{pde}} + \lambda_{\text{tv}} \ell_{\text{tv}} + \lambda_{\text{color}} \ell_{\text{color}} + \lambda_{\text{perc}} \ell_{\text{perc}}. \quad (21)$$

This final objective balances normal-image fidelity against realistic anomaly reconstruction, mitigating over-smoothing or color mismatches while preserving crucial defect features.

6.2. npcF++: Wavelet-PDE & Synergy Blocks, Dual-Branch Encoding/Decoding

Wavelet-PDE Attentive Blocks. We employ the *PDEWaveAttnBlock* to inject additional structure into feature maps. Given an input tensor $\mathbf{f} \in \mathbb{R}^{B \times C \times H \times W}$:

$$\mathbf{f}_{\text{pde}} = \mathbf{f} - \varepsilon_p \nabla^2 \mathbf{f}, \quad (22)$$

where ∇^2 is the 2D Laplacian operator and ε_p is learnable. We next decompose \mathbf{f}_{pde} into four subbands (**LL**, **LH**, **HL**, **HH**) using a discrete Haar wavelet transform:

$$\text{DWT}(\mathbf{f}_{\text{pde}}) = (\mathbf{LL}, \mathbf{LH}, \mathbf{HL}, \mathbf{HH}), \quad (23)$$

then concatenate these subbands, process them with a small convolutional layer, and perform an inverse wavelet transform:

$$\tilde{\mathbf{f}} = \text{iDWT}(\mathbf{LL}', \mathbf{LH}', \mathbf{HL}', \mathbf{HH}'). \quad (24)$$

This fusion of PDE smoothing and wavelet-domain filtering aims to capture both global coherence and fine-grained anomalies.

Boundary Synergy. Since anomalous regions often exhibit sharp transitions at the boundary, we apply a window-level cross-attention mechanism (*RegionSynergyBlock*) to combine “normal” and “anomaly” features while referencing a boundary mask \mathbf{B}_{mask} . If \mathbf{z}_N and \mathbf{z}_A are normal/anomaly feature tensors, then within each local window:

$$\mathbf{z}_N^{\text{out}} = \mathbf{z}_N + \gamma \cdot (\text{CrossAttn}(\mathbf{z}_N, \mathbf{z}_A)) \odot \mathbf{B}_{\text{mask}}, \quad (25)$$

where γ is a trainable scalar and *CrossAttn* applies single-head query-key-value attention within a local window. We interleave synergy blocks with *PDEWaveAttn* at each resolution to propagate boundary-sensitive cues through the network.

Dual-Branch Encoding and Decoding. We feed the “normal” input \mathbf{o}_N and the “anomaly” input \mathbf{o}_A into parallel encoder streams (CNN + *PDEWaveAttn*), then merge them in a shared bottleneck:

$$\begin{aligned} \mathbf{e}_N^{(1)} &= \text{EncN1}(\mathbf{o}_N), & \mathbf{e}_A^{(1)} &= \text{EncA1}(\mathbf{o}_A), \\ \mathbf{e}_N^{(2)} &= \text{EncN2}(\text{Pool}(\mathbf{e}_N^{(1)})), & \mathbf{e}_A^{(2)} &= \text{EncA2}(\text{Pool}(\mathbf{e}_A^{(1)})), \\ \mathbf{b}_N &= \text{BottN}(\mathbf{e}_N^{(2)}), & \mathbf{b}_A &= \text{BottA}(\mathbf{e}_A^{(2)}). \end{aligned} \quad (26)$$

Afterwards, we decode each stream with symmetric upsampling, *PDEWaveAttn* blocks, and synergy operations. A final 3×3 convolution plus sigmoid layer outputs the refined image \mathbf{u} .

6.3. Outer Loop: Weight’s Learning

Motivation and Overall Process. To fully exploit high-quality synthetic anomalies and suppress less realistic samples, we adopt a second-order *MAML*-like update on both the data weights $\{d_i\}$ and the final-layer parameters of the SQE network. This approach is triggered at the end of each training epoch, after we have computed the inner-loop (main model) updates.

Validation-Based Objective. Let θ' be the model parameters after the inner loop:

$$\mathcal{L}_{\text{outer}}(\theta') = \mathcal{L}_{\text{val}}(\theta'), \quad (27)$$

where $\mathcal{L}_{\text{val}}(\theta')$ typically incorporates a differentiable AUC-based metric on a small validation set. For instance, we compute a differentiable approximation of the AUC by comparing predicted scores for normal vs. anomalous samples.

Second-Order Update. We retain the computation graph from the inner loop, enabling us to backpropagate through θ' in a genuine second-order fashion. Concretely, each data weight d_i is updated via:

$$d_i^* = d_i - \eta_{\text{outer}} \frac{\partial \mathcal{L}_{\text{outer}}(\theta')}{\partial d_i}, \quad (28)$$

We then discard θ' , reverting to the original model parameters θ . Only $\{d_i^*\}$ and updated SQE parameters persist into future epochs. This ensures that each synthetic sample’s influence on validation performance is accurately reflected, amplifying beneficial anomalies while diminishing detrimental ones.

Practical Implementation Details.

- **Hyperparameters:** We use a small learning rate 10^{-4} for these weight updates to avoid over-correcting.
- **Frequency:** Typically performed after each training epoch, though less frequent updates (e.g., every k epochs) can reduce overhead.

Discussion and Benefits. Our second-order approach ensures that SQE and $\{d_i\}$ are updated in a manner that explicitly optimizes for validation performance rather than just local training loss. Consequently, **high-quality synthetic anomalies gain greater weight in subsequent epochs**, while poor-quality (overly simplistic or unrealistic) anomalies are downweighted. This adaptivity fosters a more discriminative and robust anomaly detection pipeline overall.

References. For further reading on second-order MAML and its implementation complexities, see [7, 28]. Our approach aligns with these foundational works but applies them to the domain of synthetic anomaly quality assessment.

7. Key Pseudocode for Reproducibility

In this chapter, we present detailed pseudocode for the most crucial components of our framework, aiming to facilitate straightforward reproduction of our results. By isolating core algorithms and specifying the exact data flow, we hope to clarify how each stage—from math-physics anomaly generation to coarse-to-fine refinement and final bi-level optimization—can be implemented in a typical deep-learning environment.

7.1. Generate Crack

We simulate crack formation within a specified foreground region by growing a skeleton of connected line segments, then expanding it into a realistic crack mask, as shown in Algorithms 1 and 3. Below is a concise outline:

Algorithm Overview.

1. Skeleton Initialization:

- Randomly select 1–3 starting points within the foreground mask.
- Assign each point an initial direction θ , from which we derive $dy = \sin \theta$, $dx = \cos \theta$.

2. Skeleton Growth:

- Iteratively step forward, marking skeleton pixels, until exhausting the allowed steps or hitting the boundary.
- With a small probability, `branch_prob`, generate a branch by slightly shifting dy , dx .
- Stop with probability `stop_prob` at each iteration.

3. Skeleton to Mask:

- Compute a distance transform around the skeleton.
- Threshold and optionally blend in Perlin noise to produce a crack region, applying morphological refinements.

7.2. Generate Corrosion

Corrosion is modeled as randomly placed patches that can grow and overlap, mimicking rust-like or oxidized clusters on metal surfaces or other materials. After forming these patches, we optionally add Perlin noise for a fractured, “eaten-away” visual effect, as shown in Algorithm 4 and ??.

Algorithm Overview.

1. Polygon Placement:

- Sample a set of random centers within the foreground.

Algorithm 1 GENERATESKELETON

Input: *height, width, start_points, max_steps, step_size, branching_prob, stop_prob, foreground_mask*

Output: *skeleton_mask* (binary array of size $height \times width$)

```
1: Initialize skeleton_mask to all zeros.
2: Create a queue frontiers.
3: for all  $(y_0, x_0)$  in start_points do
4:    $angle \leftarrow \text{Uniform}(0, 2\pi)$ 
5:    $dy \leftarrow \sin(angle)$ ;  $dx \leftarrow \cos(angle)$ 
6:   Enqueue  $[y_0, x_0, dy, dx, max\_steps]$  into frontiers.
7:   skeleton_mask $[y_0, x_0] \leftarrow 1$ 
8: end for
9: while frontiers not empty do
10:   $(y, x, dy, dx, steps) \leftarrow \text{frontiers.pop}()$ 
11:  if  $steps \leq 0$  then
12:    continue
13:  end if
14:   $y_{\text{new}} \leftarrow y + dy \times \text{step\_size}$ 
15:   $x_{\text{new}} \leftarrow x + dx \times \text{step\_size}$ 
16:   $y_{\text{int}} \leftarrow \text{round}(y_{\text{new}})$ 
17:   $x_{\text{int}} \leftarrow \text{round}(x_{\text{new}})$ 
18:  Check boundary or foreground:
19:  if  $y_{\text{int}}$  or  $x_{\text{int}}$  out of range or
    foreground_mask $[y_{\text{int}}, x_{\text{int}}] == 0$  then
20:    continue
21:  end if
22:  skeleton_mask $[y_{\text{int}}, x_{\text{int}}] \leftarrow 1$ 
23:   $steps \leftarrow steps - 1$ 
24:  if  $\text{Random}() < \text{stop\_prob}$  then
25:    continue
26:  end if
27:  Enqueue  $[y_{\text{new}}, x_{\text{new}}, dy, dx, steps]$  into frontiers.
28:  if  $\text{Random}() < \text{branching\_prob}$  then
29:     $\text{branch\_angle} \leftarrow \text{Uniform}(-\pi/4, \pi/4)$ 
30:     $\text{new\_dy} \leftarrow dy \times \cos(\text{branch\_angle})$ 
     $- dx \times \sin(\text{branch\_angle})$ 
31:     $\text{new\_dx} \leftarrow dy \times \sin(\text{branch\_angle})$ 
     $+ dx \times \cos(\text{branch\_angle})$ 
32:    Enqueue
     $[y_{\text{new}}, x_{\text{new}}, \text{new\_dy}, \text{new\_dx}, \lfloor \text{steps}/2 \rfloor]$ 
33:  end if
34: end while
35: return skeleton_mask
```

- Generate polygons with deformed edges and fill them into a temporary mask.
- Combine polygons into the main corrosion_mask by union or bitwise OR, depending on the overlap strategy.

2. Boundary Growth:

- Repeatedly identify boundary pixels of the current mask and convert them to foreground with probabil-

Algorithm 2 GENERATERANDOMCRACKMASK

Input: *height, width, skeleton, w_0 , α , ϵ , noise_scale, noise_octaves, morph_kernel_size*

Output: *crack_mask* (binary array of size $height \times width$)

```
1: Initialize crack_mask  $\leftarrow 0$ 
2: dist_map  $\leftarrow$ 
   distance_transform( $1 - \text{skeleton}$ )
3: noise_gen  $\leftarrow$ 
   PerlinNoise(octaves = noise_octaves)
4: for  $y \leftarrow 0$  to  $height - 1$  do
5:   for  $x \leftarrow 0$  to  $width - 1$  do
6:      $t \leftarrow \text{dist\_map}[y, x]$ 
7:      $w_t \leftarrow w_0 \exp(-\alpha t) + \epsilon$ 
8:     if  $w_t > 0$  then
9:        $\text{noise\_val} \leftarrow \text{noise\_gen}$ 
         $[y/height, x/width] \times \text{noise\_scale}$ 
10:      if  $t + \text{noise\_val} < w_t$  then
11:        crack_mask $[y, x] \leftarrow 1$ 
12:      end if
13:    end if
14:  end for
15: end for
16: MorphologicalClosing
   (crack_mask, kernel=square(morph_kernel_size))
17: MorphologicalOpening
   (crack_mask, kernel=square(morph_kernel_size))
18: blurred  $\leftarrow$  GaussianFilter(crack_mask,  $\sigma = 1.0$ )
19: crack_mask  $\leftarrow (\text{blurred} > 0.3)$ 
20: return crack_mask
```

ity grow_prob.

3. Morphological Smoothing & Noise:

- Apply morphological closing to connect separate patches.
- Optionally degrade edges using Perlin noise.

7.3. Generate Deformation

We simulate local warping or bending (*e.g.*, dents) within a designated foreground region using thin-plate spline (TPS) transformations. The core procedure involves extracting a region of interest (ROI), inpainting that ROI, then applying an RBF-based TPS displacement field to both the image and its mask, resulting in plausible deformational anomalies, as shown in Algorithm 5.

To avoid overly “stretched” deformations near object edges, we also support a TPS_DEFORM_LOCAL_INPAINT_PARTIAL variant that tries to randomly sample a sub-ROI within the foreground. This selectively warps only a portion of the region rather than the entire bounding box, reducing edge artifacts and producing more localized distortions.

Algorithm 3 APPLYCRACKTOIMAGE

Input: *orig_img*, *crack_mask*, *base_alpha*, *max_darken*, *max_color_shift*, *edge_fade*

Output: *out_img* (the BGR image with crack overlay)

```

1:  $H, W \leftarrow \text{shape}(\text{crack\_mask})$ 
2:  $\text{out\_img} \leftarrow \text{orig\_img}$  cast to float32
3:  $\text{rev\_mask} \leftarrow (1 - \text{crack\_mask})$ 
4:  $\text{dist\_map} \leftarrow \text{distance\_transform}(\text{rev\_mask})$ 
5:  $\text{crack\_strength} \leftarrow 1.0 - \frac{\text{dist\_map}}{\text{edge\_fade}}$ 
6:  $\text{crack\_strength} \leftarrow \text{clip}(\text{crack\_strength}, 0, 1)$ 
7:  $\text{crack\_strength}_3 \leftarrow \text{RepeatChannel}(\text{crack\_strength}, 3)$ 
8:  $\text{darken\_factor\_map} \leftarrow 1.0 - (1.0 - \text{max\_darken}) \times \text{crack\_strength}_3$ 
9:  $\text{color\_shift\_arr} \leftarrow \text{max\_color\_shift}$  cast to float32
10:  $\text{color\_shift\_map} \leftarrow \text{color\_shift\_arr} \times \text{crack\_strength}_3$ 
11:  $\text{cm\_bool} \leftarrow (\text{crack\_mask} == 1)$ 
12:  $\text{out\_img}[\text{cm\_bool}] \leftarrow \text{out\_img}[\text{cm\_bool}] \times \text{darken\_factor\_map}[\text{cm\_bool}]$ 
13:  $\text{out\_img}[\text{cm\_bool}] \leftarrow \text{out\_img}[\text{cm\_bool}] + \text{color\_shift\_map}[\text{cm\_bool}]$ 
14:  $\text{orig\_f32} \leftarrow \text{orig\_img}$  cast to float32
15:  $\text{out\_img} \leftarrow (1 - \text{base\_alpha}) \times \text{orig\_f32} + \text{base\_alpha} \times \text{out\_img}$ 
16:  $\text{out\_img} \leftarrow \text{clip}(\text{out\_img}, 0, 255) . \text{astype}(\text{uint8})$ 
17: return out_img

```

7.4. npcF

Our *npcF* module provides a coarse, PDE-based autoencoder framework for synthesizing anomalies. It corrects unwanted artifacts by integrating various losses (e.g., Allen-Cahn PDE, color prior, perceptual reconstruction) to yield an initial refined output. Below, we outline its core training loop in pseudocode, as shown in Algorithm 6.

In essence, **npcF** enforces a PDE-inspired correction (**Allen-Cahn**) to prevent anomaly regions from degenerating to trivial solutions (like pure black or oversmoothed patches). By simultaneously applying color and perceptual losses, we ensure that the synthesized anomalies maintain plausible tones and structures, thus forming a robust *coarse refinement stage* before more detailed enhancements in subsequent pipelines.

7.5. npcF++

Our *npcF++* stage further refines anomalies by integrating **wavelet-domain PDE blocks** and **synergy cross-attention** across multiple resolution scales. Below, we split its training procedure into two parts: the core loop (*Algo-*

Algorithm 4 GENERATECHUNKYCORROSIONMASK

Input: *foreground_mask* (binary 0/1 array)

Output: *corrosion_mask* (binary 0/1)

```

1: Initialize corrosion_mask to all zeros of shape  $(H, W)$ 
2: Extract  $\{(y_i, x_i)\}$  where  $\text{foreground\_mask}[y_i, x_i] = 1$ ; if none found, return all-zero mask
3: (A) Generate random polygons: For each polygon, pick a center  $(cy, cx)$  within foreground, define radius and angles, fill polygon to a temp mask, then combine with corrosion_mask either by union or bitwise OR depending on overlap probability.
4: (B) Local boundary growth: Repeat for a fixed number of steps:
    • Find boundary pixels by dilating corrosion_mask then subtracting it,
    • For each boundary pixel, with probability grow_prob, set it to 1 in corrosion_mask.
5: (C) Morphological closing: Apply CLOSING(corrosion_mask, kernel=square(3)) for coherence.
6: (D) Optional Perlin Noise: If enabled, sample noise  $nval \in [-1, 1]$  for boundary pixels; if  $nval > \text{threshold}$ , set those boundary pixels to 0 in corrosion_mask.
7: return corrosion_mask

```

rithm 7) and an excerpt illustrating how SYNERGYREFINETE.FORWARD combines normal/anomaly branches with boundary information (Algorithm 8). This design ensures boundary-sensitive, fine-grained anomaly generation.

In summary, **npcF++** extends beyond *npcF* by adding wavelet-based PDE blocks for multi-scale refinement and synergy cross-attention to fuse normal/anomaly features. This results in more coherent boundaries and a stronger perceptual quality in synthesized anomalies.

7.6. BiSQAD

Our *BiSQAD* framework combines a **Synthesis Quality Estimator (SQE)** with a **two-loop** optimization strategy to dynamically reweight synthetic anomalies based on their relevance to the end detection task. Below, we present two key pseudocode snippets: (1) the *inner loop* that updates the main anomaly detection model and collects per-sample losses, and (2) the *outer loop* that refines either data weights or SQE parameters via second-order gradient steps.

Explanation. In Algorithm 9, we collect per-sample losses in the *inner loop*, weighting them with a combination of $\lambda_{\text{sqe}} \cdot \text{sqe_score}$ and $\lambda_{\text{bi}} \cdot \text{data_weights}$. Then, Algorithm 10 runs a second-order update (inspired by MAML) that *locally* adapts a *temp_model*, measures validation-based

Algorithm 5 TPSDEFORMLOCALINPAINT

Input: *img_bgr* (original 3-channel image),
mask_01 (binary 0/1 foreground mask),
num_ctrl_points, *max_offset*, *dist_field_radius*, *inpaint_radius*

Output: *out_img* (deformed BGR image),
out_mask (updated binary 0/1 mask)

- 1: **Identify** $ys, xs \leftarrow \{(y, x) \mid \text{mask_01}[y, x] = 1\}$. If none found, return (*img_bgr*, *mask_01*).
 - 2: **Compute bounding box:** $(y_{\min}, y_{\max}, x_{\min}, x_{\max})$ with a small margin. Extract ROI: *roi_img* $\leftarrow \text{img_bgr}[y_{\min}:y_{\max}, x_{\min}:x_{\max}]$, *roi_mask* $\leftarrow \text{mask_01}[\dots]$.
 - 3: **Inpaint** old object pixels: *inpainted_roi* $\leftarrow \text{inpaint}(\text{roi_img}, \text{roi_mask}, \text{inpaint_radius})$.
 - 4: **Randomly select control points:** *src_pts* $\leftarrow \{(rx, ry)\} \subset \{\text{roi_mask} = 1\}$. **Offset** each by up to *max_offset* to form *dst_pts*.
 - 5: **Train RBF** (thin_plate) from *src_pts* \rightarrow *dst_pts*: *rbf_x*, *rbf_y* $\leftarrow \text{Rbf}(\text{src_pts}, \text{dst_pts}, \text{function} = \text{thin_plate}, \dots)$.
 - 6: **Compute displacement field:** For each pixel (u, v) in the ROI:

$$\Delta x \leftarrow \text{rbf_x}(u, v), \quad \Delta y \leftarrow \text{rbf_y}(u, v).$$
 Form *map_x* $\leftarrow u - \Delta x$, *map_y* $\leftarrow v - \Delta y$.
 - 7: **Remap ROI:** *warped_roi_img* $\leftarrow \text{remap}(\text{inpainted_roi}, \text{map_x}, \text{map_y})$,
warped_roi_mask $\leftarrow \text{remap}(\text{roi_mask}, \dots, \text{NEAREST})$.
 - 8: **Update ROI** in original: *new_roi* $\leftarrow \text{inpainted_roi}$; *new_roi*[*warped_roi_mask* == 1] $\leftarrow \text{warped_roi_img}[\dots]$.
 - 9: **Copy back:** *out_img* $\leftarrow \text{img_bgr}$;
out_img[*ymin*: *ymax*, *xmin*: *xmax*] $\leftarrow \text{new_roi}$.
 - 10: **Construct new mask:** *out_mask* $\leftarrow \text{zeros}(\text{mask_01})$;
out_mask[*ymin*: *ymax*, *xmin*: *xmax*][*warped_roi_mask* == 1] $\leftarrow 1$.
 - 11: **return** (*out_img*, *out_mask*).
-

auc_loss, and backpropagates to refine *data_weights*. This procedure selectively amplifies beneficial anomalies while reducing the impact of low-fidelity samples, hence improving overall detection performance.

8. Additional Details of the MaPhC2F Dataset

In the main paper, we introduced the *MaPhC2F Dataset*, a large-scale synthetic anomaly dataset spanning multiple object categories across *MVTec AD*, *VisA*, and *BTAD*. Here, we provide further details, including a per-category break-

Algorithm 6 TRAINONEEPOCH_NPCF (Core Idea)

Input: *model* (autoencoder w/ PDE constraints),
data_loader (batches of $\{\text{img}, \text{mask}, \text{stageA}\}$),
PDE & regularization hyperparameters:
eps2, *lambda_pde*, *lambda_tv*,
lambda_color, *lambda_perc*, *lambda_rec_anom*,

Output: *avg_loss* (average training loss),
optionally other stats (PDE loss, recon loss, etc.)

- 1: Initialize accumulators
total_rec, *total_pde*, *total_tv*, ... to 0
 - 2: **for each** mini-batch (*img*, *mask*, *stageA*)
in data_loader:
 - 3: **Construct input** *x_in*:
 1. If *use_stageA_img* is true, *x_in* $\leftarrow [\text{img}, \text{stageA}]$ (concatenation along channel dim)
 2. Otherwise, *x_in* $\leftarrow \text{img}$
 - 4: *recon* $\leftarrow \text{model.forward}(x_{\text{in}})$ (autoencoder output)
 - 5: **Compute normal reconstruction loss:**

$$\text{rec_loss} = \text{MSE}(\text{recon} \times (1 - \text{mask}), \text{img} \times (1 - \text{mask}))$$
 - 6: **Compute PDE-based residual** for anomaly region:

$$\text{pde_loss} = \text{MSE}(\text{AllenCahn}(\text{recon}, \text{eps2}) \times \text{mask}, \mathbf{0})$$
 (Only if anomaly pixels exist.)
 - 7: **Anomaly recon loss:**

$$\text{rec_anom} = \text{MSE}(\text{recon} \times \text{mask}, \text{img} \times \text{mask})$$
 - 8: **Total Variation:**

$$\text{tv_loss} = \text{TV_Loss}(\text{recon})$$
 (If *lambda_tv* > 0.)
 - 9: **Color prior loss:**
 - If *stageA* is provided, measure $\text{MSE}(\text{recon} \times \text{mask}, \text{stageA} \times \text{mask})$.
 - Else, compare to a constant color \mathbf{c}_{ref} .
 - 10: **Perceptual loss:**

$$\text{perc_loss} = \|\psi(\text{recon_anom}) - \psi(\text{img_anom})\|^2;$$
 - 11: **Combine all sublosses:**
 - 12: **Backward + update:**
 - 13: Accumulate each subloss in running totals.
 - 14: **Compute average losses** $\{\text{avg_rec}, \text{avg_pde}, \dots\}$ after the loop, and return or log these metrics.
-

down of the number of images generated for each type

Algorithm 7 NPCF++ Training Flow

Input: SynergyRefineNet model (dual-branch PDEWaveAttn + synergy),
 Batches of $\{b1, orig, mask\}$,
 optimizer (e.g. AdamW), wavelet penalty weight α_{wave} .
Output: Updated model parameters (fine-grained refinement).

```

1: function TRAINONEEPOCH_NPCFPP(model,
   loader, optimizer):
2:   Initialize  $total\_loss = 0$ ,  $count = 0$ .
3:   for each mini-batch ( $b1, orig, mask$ ) in loader:
4:      $out \leftarrow model.forward(orig, b1, mask)$ .
5:      $reg = REGION\_LOSS(out, orig, b1, mask)$ .
6:      $wave = WAVE\_HF\_LOSS(out, mask)$ .
7:      $loss \leftarrow reg + \alpha_{wave} \times wave$ .
8:      $total\_loss \leftarrow total\_loss + (loss \times batch\_size)$ ;
9:      $count \leftarrow count + batch\_size$ .
10:  return  $total\_loss / count$ .
```

of synthetic defect, and illustrative examples showing how *MaPhC2F* enriches existing industrial datasets with diverse anomalies.

8.1. Data Quantities per Defect Type

Tabs. 7 to 9 enumerates the total image counts for each defect category and each object class. We note that our pipeline systematically applies three physically inspired processes (crack, corrosion, TPS-based deformation) to generate varied and realistic anomaly masks. After refinement (*npcF* and *npcF++*), we accumulate the resulting synthesized images under the *MaPhC2F Dataset*.

8.2. Visualization of Synthetic Anomalies

Fig. 5, Fig. 6, and Fig. 7 depict representative samples of *MaPhC2F* images for *MVTec AD*, *VisA*, and *BTAD* categories, respectively. Each figure arranges one category per row and shows three columns corresponding to the three synthetic anomaly types:

- **Crack:** Masks grown via distance transforms and Perlin noise, emulating fracture lines.
- **Corrosion:** Chunky, “rust-like” patches with edge disruption.
- **Deformation:** TPS-based local warping or dent-like deformations.

Overall, the *MaPhC2F Dataset* contains over 115,987 synthetic images across 30 categories, serving as a valuable resource for anomaly detection. Its physically guided design yields anomalies whose shape and texture exhibit realistic correlations to real defects, while the integrated coarse-to-fine refinement process preserves rich details for training more robust detection models.

Algorithm 8 SYNERGYREFINENET.FORWARD (Excerpt)

Input: *orig* (normal input), *b1* (coarse anomaly), *mask* (binary),
 Multi-scale PDEWaveAttn & synergy blocks.
Output: *out* (refined anomaly, shape $(B, 3, H, W)$).

```

1: Encode normal:
    $eN1 = EncN1(orig)$ ;  $pN1 = PoolN1(eN1)$ ;
    $eN2 = EncN2(pN1)$ ;  $pN2 = PoolN2(eN2)$ ;
    $bN = BottN(pN2)$ .
2: Encode anomaly:
    $eA1 = EncA1(b1)$ ;  $pA1 = PoolA1(eA1)$ ;
    $eA2 = EncA2(pA1)$ ;  $pA2 = PoolA2(eA2)$ ;
    $bA = BottA(pA2)$ .
3: Decode (scale 1) + synergy:
    $upN1 = upN1(bN)$ ;
    $upA1 = upA1(bA)$ ;
    $dN1 = decN1(upN1, \dots, eN2)$ ;
    $dA1 = decA1(upA1, \dots, eA2)$ ;
    $synergy1 = synergy1(dN1, dA1, mask)$ .
4: Decode (scale 2) + synergy:
    $upN2 = upN2(synergy1)$ ;
    $upA2 = upA2(synergy1)$ ;
    $dN2 = decN2(upN2, \dots, eN1)$ ;
    $dA2 = decA2(upA2, \dots, eA1)$ ;
    $synergy2 = synergy2(dN2, dA2, mask)$ .
5: Final:
```

$$out = \text{sigmoid}(\text{final}(synergy2)).$$

return *out*.

9. Qualitative Results

In addition to the quantitative improvements demonstrated by our approach, we present a set of visual comparisons on *MVTec AD*, *VisA*, and *BTAD* to illustrate how **MaPhC2F + BiSQAD** can detect and localize anomalies more effectively, as shown in Figs. 8 to 10.

Across *MVTec AD*, *VisA*, and *BTAD*, these qualitative examples reinforce the quantitative findings presented earlier, illustrating that **MaPhC2F + BiSQAD** achieves precise, fine-grained anomaly localization even under challenging scenarios.

Defect Type	bottle	cable	capsule	carpet	grid	hazelnut	leather	metal_nut	pill	screw	tile	toothbrush	transistor	wood	zipper
Crack	627	672	657	840	792	1173	735	660	801	960	690	180	639	741	720
Corrosion	627	672	657	840	792	1173	735	660	801	960	690	180	639	741	720
Deformation	627	672	657	840	792	1173	735	660	801	960	690	180	639	741	720
Total	1254	1344	1314	1680	1584	2346	1470	1320	1602	1920	1380	360	1278	1482	1440

Table 7. Number of *MaPhC2F* images on **MVTec AD** (15 categories). Rows list defect types and total counts; columns list the individual categories.

Defect Type	candle	capsules	cashew	chewinggum	fryum	macaroni1	macaroni2	pcb1	pcb2	pcb3	pcb4	pipe_fryum
Crack	2700	1626	1350	1359	1350	2700	2700	2712	2703	2715	2712	1350
Corrosion	2700	1626	1350	1359	1350	2700	2700	2712	2703	2715	2712	1350
Deformation	2700	1626	1350	1359	1350	2700	2700	2712	2703	2715	2712	1350
Total	5400	3252	2700	2718	2700	5400	5400	5424	5406	5430	5424	2700

Table 8. Number of *MaPhC2F* images on **VisA** (12 categories). Rows list defect types and total counts; columns list the individual categories.

Defect Type	01	02	03
Corrosion	400	399	1000
TPS	400	399	998
Crack	400	399	1000
Total	1200	1197	2998

Table 9. Number of *MaPhC2F* images on **BTAD** (3 categories). Rows list defect types and total counts; columns list the individual categories.

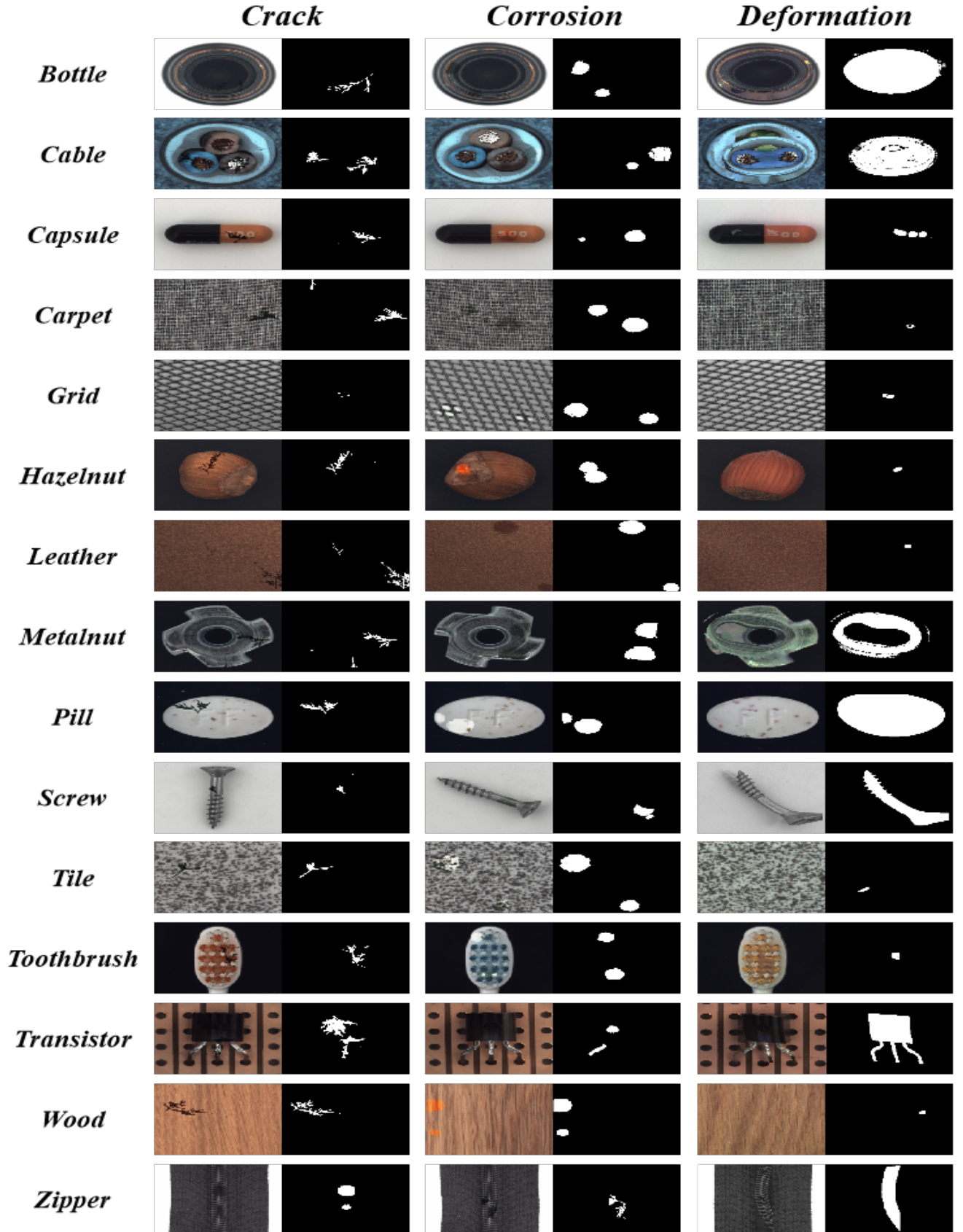


Figure 5. Examples of *MaPhC2F* anomalies on *MVTec AD* categories. Each row corresponds to one item class, and columns display crack, corrosion, and deformation, respectively.

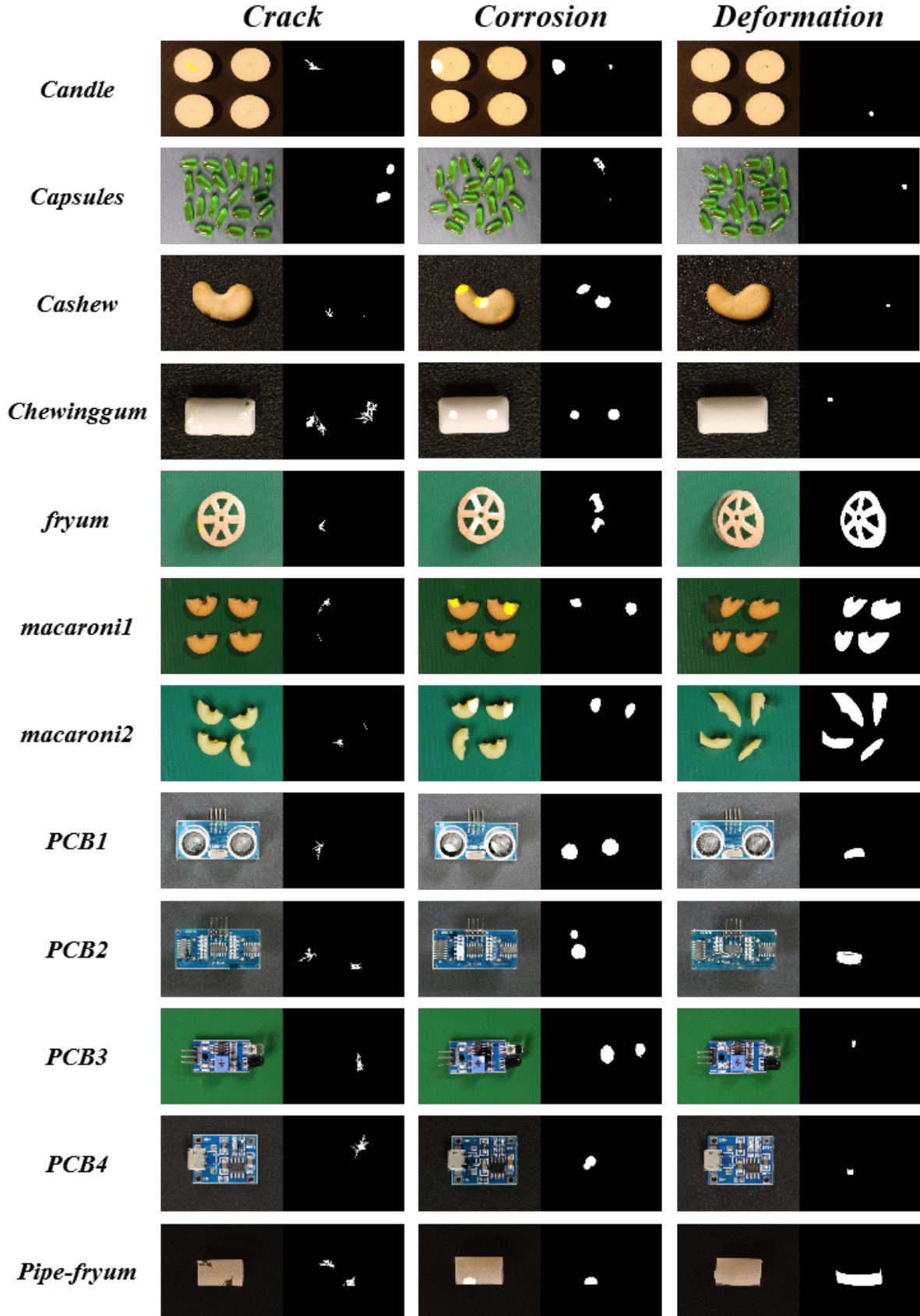


Figure 6. Anomalies synthesized for *VisA* dataset classes, visualized in the same row-by-column arrangement as Figure 5.

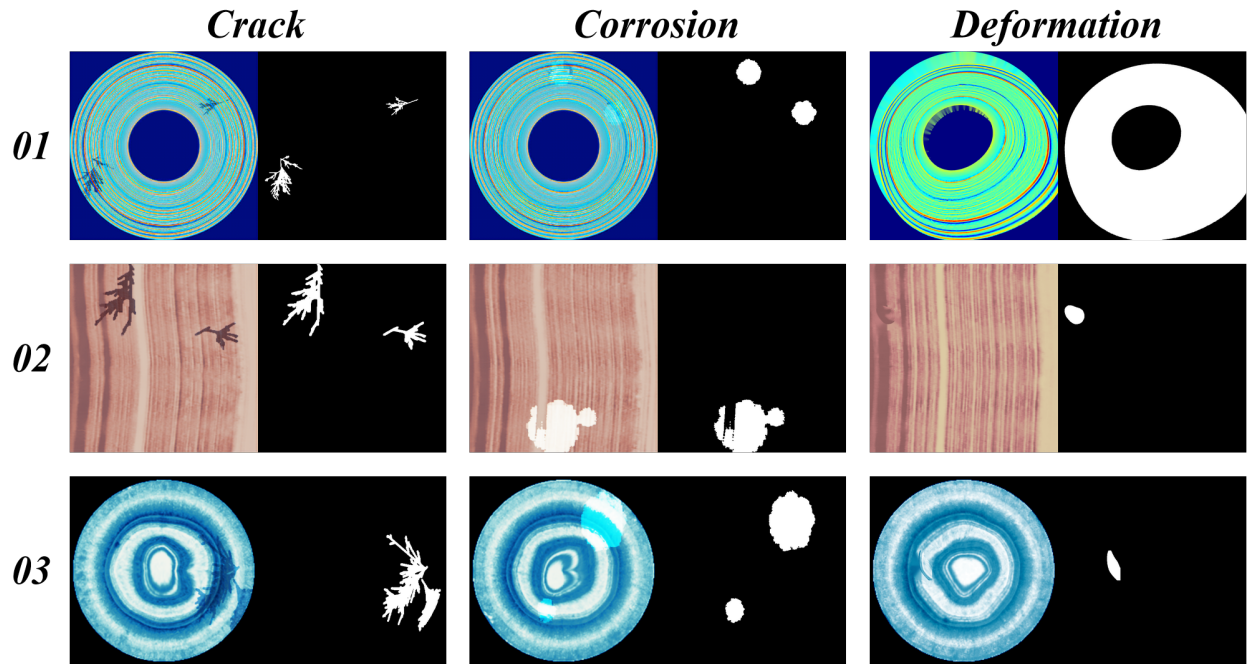


Figure 7. Additional *MaPhC2F* samples on *BTAD*, illustrating the consistency of our method across varied industrial items.

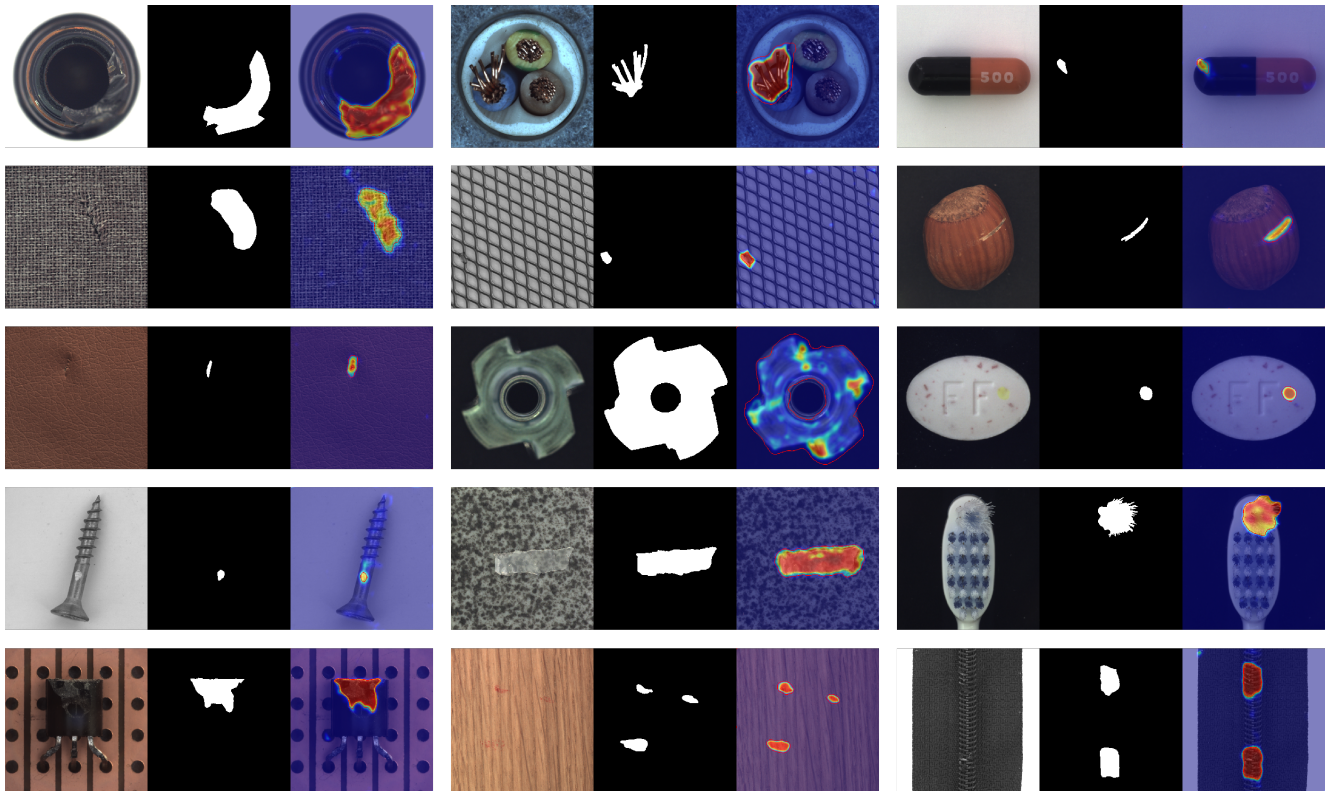


Figure 8. Visual examples of anomaly detection on several *MVTec AD* categories. Each group shows: (1) original input, (2) ground-truth mask, (3) overlay of detection results.

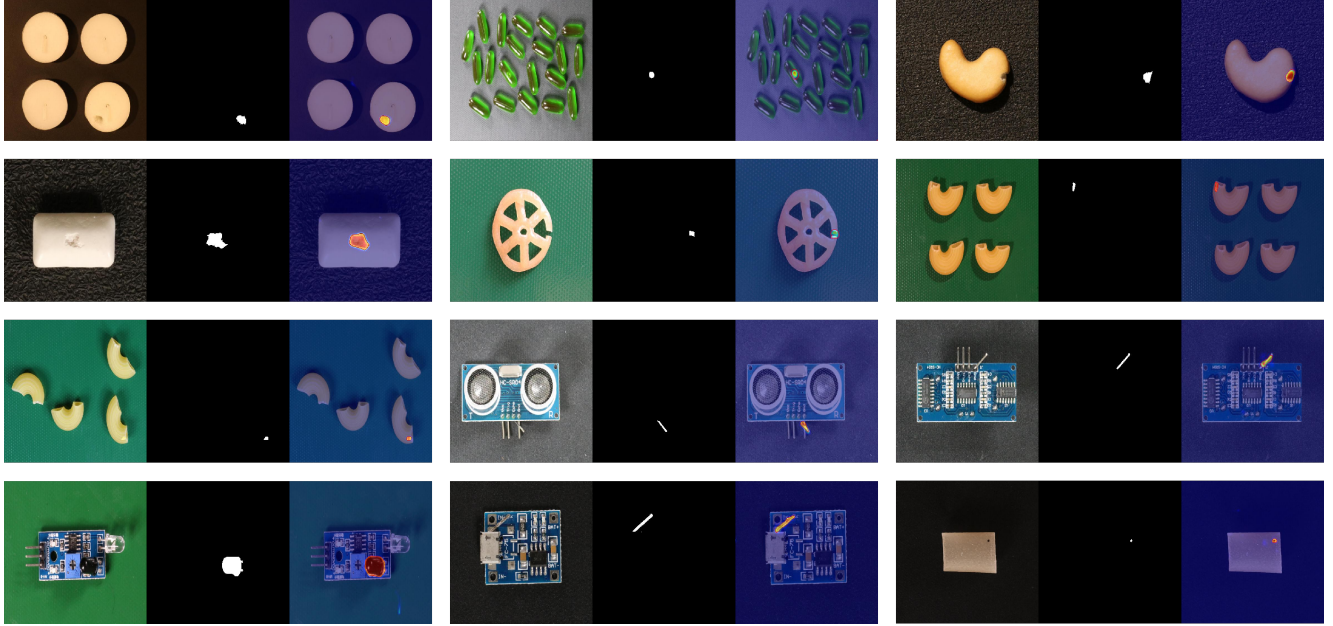


Figure 9. Visualization of detection outcomes on various *VisA* items. Our method adapts well to diverse categories.

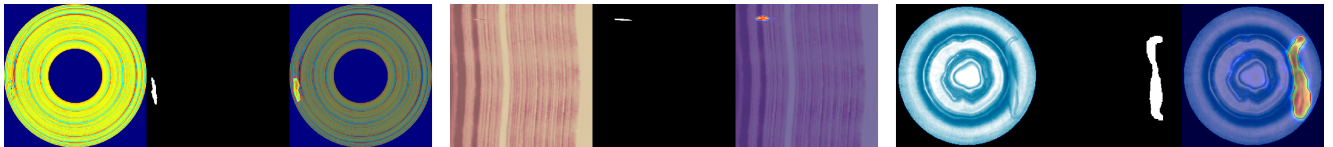


Figure 10. Examples of anomaly detection on *BTAD* data.

Algorithm 9 TRAINONEEPOCH_BISQAD (Inner Loop)

Input: **full_model** (anomaly detector),
train_loader w/ $\{image, label, img_sqe, index\}$,
optimizer,
data_weights, sqe_model (optional), $\lambda_{sqe}, \lambda_{bi}$.

Output: Updated **full_model**, and arrays of $\{index, loss_value, img_sqe\}$ for subsequent outer loop training.

```
1: function TRAINONEEPOCH_BISQAD( config,  
   train_loader, full_model, optimizer, data_weights,  
   sqe_model):  
2:   Initialize accumulators:  
    $\{epoch\_indices, epoch\_losses, epoch\_imgs\_sqe\} \leftarrow \emptyset$ .  
3:   for each mini-batch (batch) in train_loader:  
4:     outputs  $\leftarrow full\_model.forward(batch, train = True)$   
5:     Compute loss per sample:  
      $sum\_loss\_b \leftarrow \sum_{criterion \in C} (criterion.weight \times$   
        $criterion(outputs, per\_sample=True))$ .  
6:     Get SQE or data weights:  
     • If sqe_model is not None,  $sqe\_score \leftarrow sqe\_model.forward(batch.img\_sqe)$   
     • Else,  $sqe\_score \leftarrow 0$   
     •  $meta\_w \leftarrow data\_weights[batch.index]$   
     •  $final\_w \leftarrow \lambda_{sqe} \cdot sqe\_score + \lambda_{bi} \cdot meta\_w$   
     • If  $\lambda_{sqe}=0$ , fallback to uniform weighting.  
7:     Weighted total:  $weighted\_loss\_b =$   
        $sum\_loss\_b \times final\_w,$   
        $total\_loss \leftarrow weighted\_loss\_b.mean()$ .  
8:     Backward + optimize:  
9:     Accumulate for outer loop:  
      $epoch\_indices += batch.index,$   
      $epoch\_losses += sum\_loss\_b.detach(),$   
      $epoch\_imgs\_sqe += batch.img\_sqe.$   
10:  return  $\{epoch\_indices, epoch\_losses, epoch\_imgs\_sqe\}$   
    for outer loop usage.
```

Algorithm 10 OUTERLOOP_SQE (Second-Order Update)

Input: **full_model**, **data_weights**, **sqe_model**,
train_batch (a new sample), **val_loader**,
optimizer_w (for *data_weights*),
config (e.g., *meta_inner_lr, auc_alpha*).
Output: Updated *data_weights* and *sqe_model* reflecting second-order optimization.

```
1: function OUTERLOOPSQE(config, full_model,  
   data_weights, optimizer_w, train_batch,  
   val_loader):  
2:   Create temp copy: temp_model  $\leftarrow$   
   copy.deepcopy(full_model)  
3:   Inner Step:  
   1. Retrieve  $final\_w \leftarrow$   
      $data\_weights[train\_batch.index]$   
   2.  $inner\_loss \leftarrow temp\_model(train\_batch) \times final\_w$   
   3. Update temp_model w.r.t. inner_loss (using  
     meta_inner_lr).  
4:   Val AUC Loss:  
   • Evaluate temp_model on val_loader, gather  
     val_scores, val_labels.  
   • Compute AUC loss:  
      $auc\_loss \leftarrow differentiable\_auc\_loss(val\_scores,$   
        $val\_labels, \alpha = auc\_alpha)$ .  
5:   (Updates both data_weights & final layer of  
     sqe_model if attached.)  
6:   Discard temp_model, retaining only updated  
     data_weights, sqe_model.
```
